





## Systematic study of the Reynolds number and streamwise spacing effects in two-dimensional square-bar rough-wall turbulent boundary layers

Jiahao Kong <sup>1,\*</sup> Luke G. Bennetts <sup>2</sup> Bagus Nugroho <sup>3</sup> and R. C. Chin <sup>1</sup>

<sup>1</sup>*School of Mechanical Engineering, University of Adelaide, Adelaide, 5005 South Australia, Australia*

<sup>2</sup>*School of Mathematical Sciences, University of Adelaide, Adelaide, 5005 South Australia, Australia*

<sup>3</sup>*Department of Mechanical Engineering, University of Melbourne, Melbourne, 3010 Victoria, Australia*



(Received 15 July 2022; accepted 13 December 2022; published 10 January 2023)

Turbulent boundary layer experiments above a smooth wall and two-dimensional (2D) rod-roughened walls are conducted to investigate the effects of friction Reynolds numbers  $Re_\tau$  and streamwise spacing of the roughness elements on the flow properties. The first study uses the roughness pitch  $p$  to height  $k$  ratio  $p/k = 8$  and a range of friction Reynolds numbers,  $1840 \leq Re_\tau \leq 7500$ . The result shows that the drag coefficient  $C_f$  converges to the fully rough condition (akin to the classic k-type roughness at a fully developed state) with large roughness Reynolds numbers ( $k^+ > 75$ ) when the friction Reynolds number reaches  $Re_\tau \geq 3900$  and the relative roughness height is  $k/\delta_{99} \geq 0.02$ , where  $\delta_{99}$  is the boundary layer thickness. As  $Re_\tau$  increases, the premultiplied energy spectra show that the normalized energy of the near-wall cycle decreases, while the large-scale structures become more dominant. The second study uses a wide range of  $p/k$  ( $2 \leq p/k \leq 128$ ) at  $Re_\tau \approx 3500$ . The  $C_f$  and the roughness function  $\Delta U^+$  results indicate that the increase of streamwise spacing of the roughness elements  $p/k$  induces higher  $C_f$  and  $\Delta U^+$ , and it reaches the maximum value at  $p/k = 8$ . For  $p/k > 8$ , the  $C_f$  and  $\Delta U^+$  values decrease as  $p/k$  increases, indicating a less severe drag increase. The premultiplied energy spectra also show that the highly energetic near-wall cycle of streaks and quasistreamwise vortices decreases as  $p/k$  increases (for all cases from  $p/k = 2-128$ ), and they seem to be transported farther from the wall. The trend is slightly different for the largest-scale structures located around the log region. The result suggests that 2D square-bar roughness can reduce the energy distribution for the largest-scale structure for  $p/k = 2-128$ .

DOI: [10.1103/PhysRevFluids.8.014601](https://doi.org/10.1103/PhysRevFluids.8.014601)

### I. INTRODUCTION

Surface roughness is a common feature in various applied and practical flows, such as rivet-joint surfaces of aircraft wings [1], recently cleaned ship hulls [2,3], biofouling of ship-hulls [4,5], and sea ice cover on the ocean surface [6]. It is known to create higher wall drag than a smooth wall, a feature that can be observed in the vertical downward shift of a streamwise mean velocity profile. The shift is commonly known as the roughness function  $\Delta U^+$  [7], where  $U$  is the mean streamwise velocity, the superscript  $+$  indicates the scaling of viscous units, namely, the friction velocity  $U_\tau$ . The  $U_\tau$  can be used with the free-stream velocity  $U_\infty$  to calculate the local coefficient of friction  $C_f = 2(U_\tau/U_\infty)^2$ , which is important for drag estimation in various applications. Surface roughness is also an important design parameter for turbulent boundary layers (TBLs) because it can influence various characteristics, such as heat transfer, momentum transport, and even flow control [8]. A wide range of surface roughness types has been investigated over the past nine decades. However,

\*[jiahao.kong@adelaide.edu.au](mailto:jiahao.kong@adelaide.edu.au)

the influence of different roughness geometries on the friction drag, mean velocity profiles, and turbulent mixing properties remains unclear and challenging to study [9–11]. Recently detailed laboratory and computational fluid dynamics (CFD) studies have shown that various types of surface properties can contribute to the flow dynamics, including roughness height  $k$ , effective slope, skewness distribution patterns, and solidity [2,11–16]. The large range of possible roughness topologies has raised the need to classify roughness, with some well-known examples being the classic equivalent sand-grain roughness height  $K_s^+ = K_s U_\tau / \nu$  [17], where  $\nu$  is the kinetic viscosity, and the combination of local  $C_f$  isotropy and spanwise homogeneity of  $C_f$  [18].

In its simplest form, surface roughness can be differentiated into two-dimensional (2D) and three-dimensional (3D) roughness. The former (2D) is commonly associated with simple elements (circular rods or rectangular bars) aligned at right angle to the flow direction, while the latter (3D) is typified by sand-grain type roughness. 3D roughness has been investigated extensively due to its similarity to realistic roughness [11,19,20]. 2D regular roughness are characterized by uniform roughness elements, with regularly streamwise distribution, which are used as simplified models to study roughness effects, e.g., of sea ice on the ocean surface [21,22]. Their cross-sectional shape and streamwise arrangement of the roughness elements are particularly important on influencing heat and momentum transfer performance [14,23,24]. For conciseness, only 2D regular roughness will be discussed in this study, which refers to 2D roughness. Early experimental investigations of TBLs over 2D rough walls consisted of regular streamwise arrangements of circular rods or rectangular bars [25–27]. Many of these early studies form the basis of our understanding of rough-wall turbulent flows. One such study is the seminal work of Perry *et al.* [28] where they classify 2D roughness into two types, namely, d-type and k-type roughness. The k-type roughness is known to have similar properties and behavior as sand-grain type roughness of Nikuradse [17], whereas flow behaviors for d-type roughness correlate with the outer length scale, e.g., the boundary layer thickness  $\delta_{99}$  for TBLs and the pipe diameter  $d$  for pipe flows. To simplify the d-type and k-type roughness differentiation and by-passing the expensive experiment to check whether a 2D surface roughness is a d-type or k-type, Tani [29] defines d-type roughness as closely spaced roughness elements (e.g., rods) with a pitch ratio  $p/k < 4$  (where  $p$  is the streamwise spacing of adjacent elements), whereas k-type roughness has widely spaced roughness elements with  $p/k > 4$ . However, this simplified definition is not universally accepted, and subsequent reports indicate other roughness properties affect the rough-wall flow dynamics and cause the roughness to behave as d- or k-type. Leonardi *et al.* [30] indicated that the differences between d-type and k-type roughness are due to the different magnitudes of the viscous drag and pressure drag. They also suggested that the d-type roughness is observed when the origin of the wall-normal location is on the crests plane and the frictional drag is larger than the pressure drag.

Despite the progress made, the physics behind flows over rough walls is still unclear, especially on how the outer layer length scale (e.g., the boundary layer thickness,  $\delta_{99}$ ) affects the increase in  $\Delta U^+$ , particularly for d-type roughness [31]. Several experimental and numerical reports revealed a form of pseudorandom ejection or outflows of fluids from the valley between two roughness elements into the upper flows [27,32–35]. Other authors suggest the existence of small roller vortices within the 2D roughness valleys that are isolated from the upper flows and act like a 2D lid-driven cavity flow, while the upper flow would experience minimal disturbance and experience alternating slip- and no-slip-like boundary condition at the interface [28,36,37]. These schools of thought are based on the fact that most of the available experimental and numerical investigations were conducted over spanwise-aligned bars with a relatively low pitch ratio ( $p/k < 1$ ). This situation raises a question about the influence of the bar height towards the ejection of fluids from the cavity. A recent minimal-span roughness channel DNS study by Macdonald *et al.* [31] indicates that increasing the bar height while keeping the gap length between the bars fixed in viscous units will result in non-k-type roughness behavior, even though it does not always end up in d-type roughness. For a deep cavity, they also found that  $\Delta U^+$  appears to depend only on the gap length in viscous units because the flow is no longer affected by the depth of cavities and instead can be influenced significantly by the length of the gap between the bars.

Based on the understanding of the behavior of k- and d-type roughness, the pitch ratio ( $p/k$ ) is one of the most significant parameters affecting the dynamics of 2D roughness TBLs. One of the earliest systematic studies of 2D roughness TBLs was conducted by Furuya *et al.* [23], in which they analyzed various pitch ratios of circular rods ( $p/k = 1, 2, 4, 8, 16, 32,$  and  $64$ ) in a wind tunnel and found that the flow's resistance is strongly influenced by the pitch ratio. The drag increases with  $p/k$ , where it reaches the maximum drag (highest  $\Delta U^+$ ) at  $p/k = 8$  and then it starts to decrease as  $p/k > 8$ . This result was later supported by other parametric studies, particularly from DNS studies [30,35,38,39].

Townsend's outer-layer similarity hypothesis [40] is a critical concept in the study of surface roughness, which states that above the roughness sublayer and at a sufficiently large Reynolds number, turbulent flows are independent of the configuration of the surface roughness. Jiménez [10] suggested that when the roughness height  $k$  is relatively small to the boundary layer thickness  $\delta_{99}$ , such that  $\delta_{99}/k \geq 40$  (note that  $\delta_{99}/k$  can also be identified as the ratio of boundary layer to roughness length scales), rough-wall TBLs demonstrate the outer-layer similarity. Several other studies on flows over 2D roughness support the outer-layer similarity hypothesis, such as the symmetrically roughened channel flows (where the top and lower walls are covered with 2D rectangular bars or circular rods) [41,42]. Experimental results by Bakken *et al.* [41] show that symmetrically roughened channel flows covered by 2D rectangular bars indeed obey the outer-layer similarity hypothesis. They also predicted a similar outcome for symmetrically roughened pipe flows. Their results are strengthened by the joint experimental and direct numerical simulation (DNS) results of Krogstad *et al.* [42] and DNS results of Ashrafiyan *et al.* [43] and Ashrafiyan and Andersson [44]. However, many reports have shown a contradictory view on the outer-layer similarity hypothesis over the 2D roughness wall-bounded flow, particularly for the asymmetrical channel flow (where only one side wall rough) and developing boundary layer [13,19,34,39,45]. Faced by these opposing views, Krogstad *et al.* [42] and Lee and Sung [34] speculate that roughness effects for the outer layer, particularly those that are caused by 2D roughness, may be dependent on the flow type. Notably, some of the similarity breakdowns happen even when the 2D roughness TBL over spanwise-aligned rods having a small pitch ratio  $p/k = 4$  at a friction Reynolds number  $Re_\tau \approx 2000$  and  $\delta_{99}/k \approx 47$  [19], which is higher than the limit set by Jiménez [10]. To address much of the conflicting information in the literature, Efros and Krogstad [46] conducted a 2D roughness boundary layer experiment over a wide range of friction Reynolds numbers ( $Re_\tau = 4200$ – $13\,300$ ), where, for the highest  $Re_\tau$  case, the roughness has a large value of the ratio  $\delta_{99}/k \approx 130$ . Their results indicate that the outer-layer similarity hypothesis is preserved, stipulating that an increase in scale separation ratio and Reynolds number provide a significantly different conclusion. A more recent DNS simulation of 2D roughness bars on spatially developing TBLs by Choi *et al.* [47] also shows that wall similarity in the outer layer is achieved when the roughness has a large ratio of  $\delta_{99}/k \approx 250$ . Note that most DNS studies investigating the effects of  $p/k$  were conducted at a relatively low friction Reynolds number ( $Re_\tau \approx 180$ – $600$ ) and low  $\delta_{99}/k$ , i.e.,  $\delta_{99}/k = 5$  [30,38],  $\delta_{99}/k = 16$ – $20$  [39],  $\delta_{99}/k = 20$ – $22$  [35]. These results indicate a departure from the outer-layer similarity hypothesis. The effect of the pitch ratio and the existence of the outer-layer similarity hypothesis for flows with higher friction Reynolds numbers  $Re_\tau$  and higher  $\delta_{99}/k$  are unknown.

Coherent turbulent structures (or eddies) are another critical aspect in the study of TBLs over 2D roughness, as their dynamic properties control fundamental mechanisms of heat and momentum transfer. However, there are limited studies in the literature about the coherent structure of turbulent flow over 2D roughness, particularly at high friction Reynolds numbers  $Re_\tau \approx 3000$  [48]. This situation is in contrast with canonical smooth-wall-bounded flows (turbulent boundary layer, turbulent channel flow, and turbulent pipe flow) that have received considerable attention since the early 1950s, particularly in terms of near-wall structures, hairpin structures/packets, and attached eddies (see also the reviews on coherent structures in canonical wall-bounded flows, including the recently discovered large-scale structures and very large-scale structures and superstructures [49–55]). Studies of coherent turbulent structures over 2D roughness have gained momentum since the early 2000s, with the emergence of the particle image velocimetry (PIV) technique [50,51,56].

PIV studies on 2D roughness reveal coherent structures in the form of vortices with a size close to the roughness elements [48,57–60]. Further, DNS analysis on this type of roughness shows highly turbulent vortical structures and hairpin packets above the roughness peak akin to a canonical wall-bounded flow [39,61]. These 2D roughness studies ultimately led to the detection of the very large-scale coherent motions or “superstructures” that have been found to dominate within high Reynolds number TBLs [51,62,63]. Recent DNS studies by Nadeem *et al.* [35], Lee *et al.* [39] and Choi *et al.* [47] reveal the telltale signs of superstructures on a spatially developing (TBLs) over 2D roughness in the form of very long negative streamwise velocity fluctuations (between  $5\delta$  and  $10\delta$ ) and an outer peak in the premultiplied energy spectra of the streamwise velocity fluctuation, despite the fact that the simulations were conducted at a low friction Reynolds number ( $Re_\tau \approx 150$ – $700$ ). These DNS results raise further questions about superstructures over 2D roughness TBLs at high Reynolds numbers, particularly due to the fact that superstructures are known to leave footprints at the surface that modulate the near-wall structure [63]. To the best of authors’ knowledge, there are not many studies looking into this matter for 2D roughness TBLs at higher Reynolds numbers.

From the discussions above, for 2D roughness it seems that there are three important parameters affecting the flow dynamics: the pitch ratio  $p/k$ , the ratio of  $\delta_{99}/k$ , and Reynolds number. The effects of the pitch ratio on 2D roughness TBLs at low  $Re_\tau$  have been investigated using DNS by Lee *et al.* [39] and Nadeem *et al.* [35]. The influences of the pitch ratio remain unknown for higher- $Re_\tau$  2D roughness TBLs on the mean statistics, dynamics features, and coherent structures. In the present study, we used laboratory experiments to investigate the influence of 2D square-bar roughness on the turbulence statistics, with respect to the Reynolds number and the streamwise spacing effects (or the pitch ratio). Hot-wire anemometry (HWA) TBL experiments were performed over 2D square-bar roughness. First, we investigated the influence of Reynolds numbers on the critical pitch ratio of  $p/k = 8$ , which is known to generate the highest drag (the highest increase in  $\Delta U_\tau$ ). To observe the streamwise spacing behavior spanning a wide range of  $p/k$  at higher Reynolds number, a set of experiments were performed over 2D square-bar roughness with  $p/k = 2$ – $128$ . For the Reynolds number matching purpose, all measurements were performed at different free-stream velocities over approximate development lengths  $x \approx 1.5$  m. The measurement location varies because it needs to be constrained at the midpoint between two adjacent roughness bars. Finally, the influence of 2D roughness on the naturally occurring superstructures was investigated by analyzing the energy spectrum and the autocorrelation profiles.

## II. EXPERIMENTAL DETAILS

Throughout this paper, the Cartesian coordinates  $x$ ,  $y$ , and  $z$  refer to the streamwise, wall-normal, and spanwise directions, respectively, with corresponding velocity components  $U$ ,  $V$ , and  $W$ , where  $y$  is defined as the wall-normal distance from the bottom wall for rough-wall measurements. The boundary layer thickness  $\delta_{99}$  is the distance from the wall to the position where  $U/U_\infty = 0.99$ . The viscous length scaling is made by the wall unit  $l_v = \nu/U_\tau$ , for instance,  $y^+ = yU_\tau/\nu$ . The friction velocity is defined as  $U_\tau = \sqrt{\tau_w/\rho}$ , where  $\tau_w$  is the wall shear stress and  $\rho$  is the fluid density, which is a key scaling parameter and determined by two techniques for smooth- and rough-wall TBLs, as discussed in Sec. II E.

### A. Facility

Experiments were conducted in the closed-loop wind tunnel at the University of Adelaide. The wind tunnel can be operated up to a maximum speed of  $30 \text{ m s}^{-1}$ . The flow goes through three layers of meshes and one layer of honeycomb grid, and then comes out from a square cross-sectional outlet of  $0.5 \times 0.5 \text{ m}^2$ , which can maintain a low turbulence level of approximately 0.5%. The wind tunnel has a 2 m length working section with a rectangular cross-sectional area of  $0.5 \times 0.3 \text{ m}^2$ . The sidewalls of the test section are fully adjustable for pressure gradient adjustment. To accelerate the turbulent flow development spatially, a tripping device consisting of a 3 mm diameter threaded rod and a 36 grit sandpaper of length 100 mm was applied at the inlet of the test section.

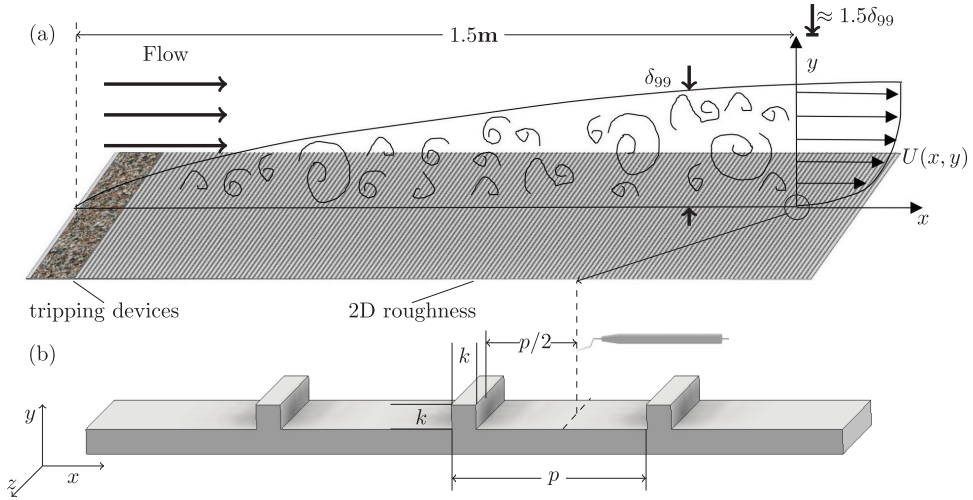


FIG. 1. Schematic views of square-bar surfaces and the measurement location.

### B. Smooth and rough walls set-up

In this study, two types of surfaces were investigated and compared, smooth surface and rough surface, that comprise various 2D square-bar setups. For the smooth surface/wall case, the surface was made of 1.6 mm thick polished aluminum plate covering the entire floor of the test section. The aluminum plate was chamfered at the leading edge with a gentle slope to avoid any step effect, and the tripping devices were attached at the beginning of the plate. The rough surfaces were made by affixing spanwise square bars made from ABS plastic, with a height of 1.5 mm on the same aluminum plate used for the smooth-wall TBL measurement. Figure 1 shows a schematic view of the square-bar arrangement and the definition of pitch and roughness height. A wide range of pitch-to-height ratios  $p/k$  from 2 to 128 was achieved by varying the bars' streamwise spacing  $p$ . The name of each rough-wall case is shown in the first column of Table II below, indicating the pitch ratio: for example, pk2 denotes the case of TBL over square-bar surfaces with  $p/k = 2$ .

### C. Hot-wire anemometry

The boundary layer velocity measurements for smooth- and rough-wall TBLs were taken using hot-wire anemometry (HWA). The HWA is an in-house designed constant temperature anemometer following the design of Perry and Chong [64]. All results were obtained using single-wire boundary-type probes with prong tips spacing of 2 mm. Platinum-Wollaston wires were soldered to the prong tips and etched to produce a sensor filament of  $d = 2.5 \mu\text{m}$  diameter and  $l = 0.51 \text{ mm}$  length, which gives the length-to-diameter ratio  $l/d \geq 200$ . The ratio is deemed suitable to minimise attenuation due to end conduction by Ligrani and Bradshaw [65] and Hutchins *et al.* [66]. The constant-temperature anemometer overheat ratio was set to be 1.8, which can be defined as  $R_w/R_a = 1.8$ , where  $R_a$  is the cold resistance of the sensor, and  $R_w$  is the operating resistance. The system's frequency response was set at approximately 18 kHz when the probes are experiencing a zero free-stream flow. For all results shown in this paper, the hot-wire analog output was sampled with frequency  $f_s = 51\,200 \text{ Hz}$  and a minimum duration  $T = 120 \text{ s}$  using a National Instrument data acquisition board (USB-NI6211). The viscous sample time interval is  $t^+ = 1/f_s(U_\tau^2/\nu)$ , following the recommended value of  $t^+ < 3$  to capture all the relatively high-energy content frequency [66]. Note that the largest scale of turbulence structures are observed to exceed  $20\delta$  [63,67], hence, the sampling duration is required to encompass several hundreds of these large-scale events for the converged statistics ( $TU_\infty/\delta_{99} > 20\,000$ ). Based on Table II below, all results satisfy the temporal

TABLE I. Detail of TBL parameters for a 2D rough wall with matched pitch ratio of  $p/k = 8$ .

Case	$p/k$	$U_\infty$ ( $\text{ms}^{-1}$ )	$U_\tau$ ( $\text{ms}^{-1}$ )	$\delta_{99}$ (mm)	$\epsilon$ (mm)	$C_f$	$\Delta U^+$	$\text{Re}_\tau$	$\delta_{99}/k$	$\delta_{99}/K_s$	$l^+$	$t^+$	$TU_\infty/\delta_{99}$	Symbol
pk8A	8	6	0.377	73.5	1.15	0.00778	10.14	1840	49.0	9.59	12.7	0.18	$10 \times 10^3$	□
pk8B	8	9.2	0.562	73.8	1.06	0.00744	10.69	2680	48.9	9.63	18.9	0.41	$15 \times 10^3$	□
pk8C	8	12.8	0.755	79.7	1.02	0.00699	11.20	3900	53.1	10.40	25.4	0.73	$19 \times 10^3$	□
pk8D	8	16	0.940	79.9	0.88	0.00686	11.53	4950	53.3	10.43	31.6	1.14	$24 \times 10^3$	□
pk8E	8	24	1.421	80.8	0.91	0.00694	12.54	7500	53.9	10.55	47.8	2.60	$36 \times 10^3$	□

performance criteria in  $t^+$  and  $TU_\infty/\delta_{99}$ . In terms of spatial resolution, since the viscous scale  $\nu/U_\tau$  varies with free-stream velocities, the inner-scaled wire length  $l^+ (= lU_\tau/\nu)$  will also vary from 24 to 47. Therefore, the measurements will experience some forms of attenuation due to insufficient spatial resolution, particularly at the higher end of the free-stream velocities [66].

The hot-wire sensors are statistically calibrated against a Pitot tube located above the hot-wire probes, approximately 10 mm into the free-stream flow. Calibrations were made before and after each wall-normal boundary layer traverse (pre- and postcalibration). The free-stream velocity was determined by the difference between the total and static pressures from the Pitot-tube and monitored by an electronic barometer (220DD Baratron, MKS). The flow temperature was also monitored by a calibrated RTD-type thermocouple (Pt1000). Fourth-order polynomial curves were used to fit the pressure data and hot-wire voltage signals. Linear interpolation was made to correct the temperature drift between pre- and postcalibration. In addition, the free-stream velocity was recorded throughout each traverse station and used to compare with the hot-wire signals in the free-stream flow. The whole set of data was discarded if the difference of  $U_\infty$  from the pressure data and hot-wire signals is larger than  $\pm 1\%$  [66].

#### D. Experiments

The zero pressure gradient TBLs were measured from the near-wall location to the free-stream flow at  $y = 1.5\delta_{99}$  using a 1D traverse system. The traverse system comprised a Mitutoyo height gauge, driven by a micron stepper motor and controlled by an optical linear encoder. The smooth-wall TBL measurement was performed at  $x = 1.5$  m downstream from the tripping devices and free-stream velocity  $U_\infty = 20$  m  $\text{s}^{-1}$  to achieve friction Reynolds numbers,  $\text{Re}_\tau = 1900$ . As shown in Fig. 1, all rough-wall measurements were conducted at approximate streamwise locations of  $x \approx 1.5$  m, close to where the smooth-wall TBL was obtained. The actual streamwise positions were varied because the rough-wall measurements were taken at the midpoint between two roughness elements in the streamwise direction for all rough-wall cases as in the previous studies by Lee *et al.* [39] and Nadeem *et al.* [35]. The present study also focuses on the influence of various  $\text{Re}_\tau$  at just one particular  $p/k$  ratio, namely  $p/k = 8$  because it is extensively investigated as a classic k-type roughness inducing the highest drag coefficient to TBLs in respect to others pitch ratios. The  $\text{Re}_\tau$  was varied by changing the wind tunnel's free-stream speed from 6 to 24 m  $\text{s}^{-1}$  (see Table I for further details). Subsequently, the rough-wall measurements were run at a range of free-stream velocities  $U_\infty = 12$ –24 m  $\text{s}^{-1}$  over various pitch ratio cases, where the velocity for each rough-wall case was chosen to achieve similar friction Reynolds numbers,  $\text{Re}_\tau \approx 3500$ . The experimental conditions and important flow parameters for the smooth and the rough walls with different  $p/k$  are summarized in Table II.

The smooth-wall results are compared with that of a DNS study [68] at a similar friction Reynolds number  $\text{Re}_\tau \approx 2000$ . Figure 2 shows the mean velocity and the normalized turbulence intensity profiles in the inner-scaled coordinate. The present result collapses well with the DNS data in the mean velocity profile at all positions. The normalized turbulence intensity profiles also show a good agreement with the DNS results above the log region ( $y^+ > 100$ ). The smaller peak value of

TABLE II. Detail of smooth-wall and 2D rough-wall TBL parameters at various pitch ratios  $p/k$  where the rough-wall cases have matched friction Reynolds numbers of  $Re_\tau \approx 3500$ .

Case	$p/k$	$U_\infty$ ( $ms^{-1}$ )	$U_\tau$ ( $ms^{-1}$ )	$\delta_{99}$ (mm)	$\epsilon$ (mm)	$C_f$	$\Delta U^+$	$Re_\tau$	$\delta_{99}/k$	$\delta_{99}/K_s$	$l^+$	$t^+$	$TU_\infty/\delta_{99}$	Symbol
Smooth	–	20	0.746	38.3	–	0.00279	–	1930	–	–	25.1	0.72	$63 \times 10^3$	○
pk2	2	23.7	1.084	48.0	1.57	0.00416	5.95	3460	32.0	71.39	36.5	1.51	$60 \times 10^3$	□
pk4	4	17	0.916	60.5	1.22	0.00583	9.80	3800	40.3	17.69	30.8	1.08	$34 \times 10^3$	◻
pk8	8	12.8	0.755	79.7	1.02	0.00699	11.20	3900	53.1	10.40	25.4	0.73	$19 \times 10^3$	◻
pk12	12	13	0.737	72.2	1.08	0.00647	10.27	3500	48.1	12.39	24.8	0.70	$22 \times 10^3$	◻
pk16	16	14.4	0.808	68.2	0.51	0.00626	10.07	3600	45.5	13.94	27.2	0.84	$25 \times 10^3$	◻
pk24	24	16.1	0.846	66.2	0.31	0.00601	9.62	3730	44.1	17.00	28.4	0.92	$29 \times 10^3$	◻
pk48	48	19	1.013	58.1	0.11	0.00572	9.27	3860	38.7	20.66	34.1	1.32	$43 \times 10^3$	◻
pk96	96	22.3	1.112	46.6	0.10	0.00498	7.85	3370	31.0	32.50	37.4	1.59	$57 \times 10^3$	◻
pk128	128	23.7	1.104	46.5	0.08	0.00433	6.29	3340	31.0	61.28	37.2	1.57	$61 \times 10^3$	◻

the experimental results in turbulence intensity is attributed to the attenuation of small turbulence motions due to large  $l^+$  [66,69]. In particular, Hutchins *et al.* [66] conducted a smooth-wall TBL experimentally with  $l^+ = 22$  at a similar friction Reynolds number  $Re_\tau \approx 2000$ . Their results showed a similar peak magnitude of normalized turbulence intensity at  $y^+ \approx 15$ .

### E. Friction velocity estimation

The evaluation of friction velocity  $U_\tau$  is important because it is used to normalize the streamwise mean velocity profile and to determine the friction drag coefficient  $C_f$ . Estimating  $U_\tau$  in experiments is challenging due to the lack of an independent measure of the wall-shear stress  $\tau_w$ . For the smooth-wall TBL, the composite profile method, developed by Chauhan *et al.* [70], is used to determine  $U_\tau$  and  $\Pi$  simultaneously, as the method uses all measurement points to fit with the reference profile, making it robust. It is based on a composite function comprising of the Musker function for the inner region and an exponential function for the wake region to fit with all the measurement points, as shown in the Appendix. This method is compared with a well-known technique, the Clauser method [71], which fits the measured smooth-wall mean velocity profile onto the log region by adjusting  $U_\tau$

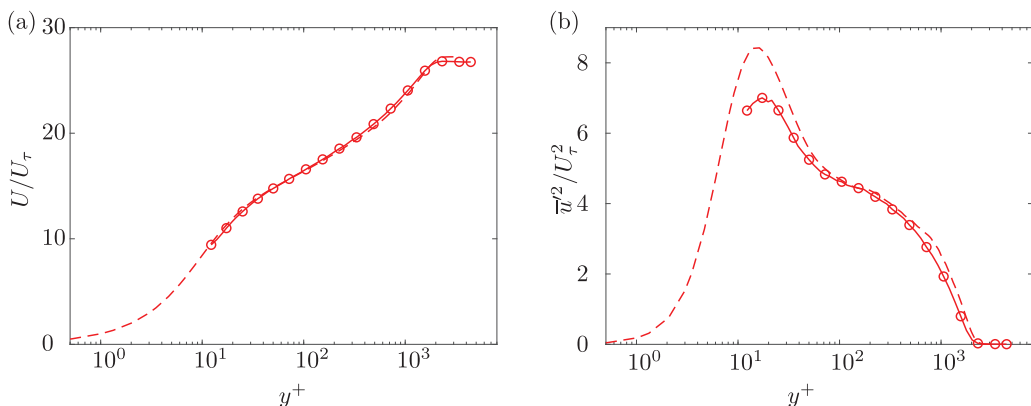


FIG. 2. Comparison of the present smooth-wall and the DNS smooth-wall results at  $Re_\tau \approx 2000$  [68]. Inner-scaled mean velocity profile (a); inner-scaled turbulence intensity profile (b). Dash line, the DNS smooth-wall result [68]; circle, the present smooth wall.

as in

$$U^+ = \frac{1}{\kappa} \ln(y^+) + B, \quad (1)$$

where  $\kappa$  and  $B$  are known as the von Kármán constant and the intercept constant. The  $\kappa$ - and  $B$ -values are believed to be independent of the wall condition, here taken to be 0.41 and 5.3 for the smooth-wall and 2D rough-wall TBLs [13,39,46]. The fitting process also requires properly defined bounds of the log region, which are suggested at  $y_{\text{inner}}^+ = 3\sqrt{\text{Re}_\tau}$  and  $y_{\text{outer}}^+ = 0.15\text{Re}_\tau$  for smooth-wall TBLs by Marusic *et al.* [72]. The resulting  $U_\tau$  between the two methods are found to be very similar, with a difference about 2%. Note that the  $\kappa$  value is suggested to be  $\kappa = 0.384$  for the smooth-wall TBL by Chauhan *et al.* [70]. We performed the above two techniques with  $\kappa = 0.384$  for the present smooth-wall data to investigate the uncertainty caused by the  $\kappa$  value. The difference between two new estimated  $U_\tau$  is less than 2%. Comparing the  $U_\tau$  from the composite profile method using  $\kappa = 0.384$  and 0.41, the deviation is around 1%. This outcome indicates that the  $U_\tau$  estimation technique for the smooth-wall data, the composite profile method is insensitive to the  $\kappa$  value.

For rough-wall measurements, determining  $U_\tau$  is even more challenging due to the introduction of two additional unknowns, namely the roughness offset  $\epsilon$  and the Hama roughness function  $\Delta U^+$  [7,10,28,73]. The roughness offset  $\epsilon$  accounts for the fact that the roughness displaces the entire flow away from the bottom wall. The wall-normal position from the virtual origin is defined as  $y^* = y - \epsilon$ . The classic method to obtain  $U_\tau$ ,  $\epsilon$ , and  $\Delta U^+$  in a rough wall is via the modified Clauser method [26] (see the Appendix). However, the uncertainty in determining the range and limit of the log-region makes it difficult to estimate  $U_\tau$  and  $\Delta U^+$  accurately [74]. Flack *et al.* [74] reported that the uncertainty of estimating  $U_\tau$  using mean velocity profile via Clauser or modified Clauser method (for the rough-wall cases) is around 3%–5%. Furthermore, Schultz and Myers [75] illustrate that the experimental error in estimating  $\Delta U^+$  varies between 6%–16%. Apart from finding  $\Delta U^+$  and  $U_\tau$ , the third component that needs to be determined is the roughness offset  $\epsilon$ . The roughness offset  $\epsilon$  is usually set at the median height of roughness ( $\epsilon = 0.48k$ ) for 2D roughness with  $p/k = 8$  [13,34,38]. However, it is not applicable to use a constant  $\epsilon$  for all the rough-wall measurements ranging from  $p/k = 2$ –128 as suggested by Leonardi *et al.* [38]. Using a median roughness height on the present rough-wall results would cause an abnormal mean velocity profile. We follow Perry and Joubert [26] and Perry *et al.* [28], where  $\epsilon$  was obtained via iteration on the modified Clauser method. The procedure was initialised with the  $U_\tau$  estimate given by the modified Clauser method [26]. In this method,  $U/U_\infty$  was plotted as a function of  $y^*/\delta^*$ , where  $\delta^*$  is the displacement boundary layer thickness. By applying various  $\epsilon$  to the experimental data, several iterations were made by applying the first-order polynomial fit to evaluate a constant line that can do the best fit to the log region of the reference profile, which is defined from  $y^{*+} = 200$  to  $y^*/\delta_{99} = 0.2$  [76,77]. According to Eq. (A5), the slope of the constant line is equal to  $\frac{1}{\kappa} \frac{U_\tau}{U_\infty}$ . Then the best combination of  $U_\tau$  and  $\epsilon$  was determined, where the  $\epsilon$  values are listed in Table I and II. The origin offset  $\epsilon$  was applied to the wall-normal position data.

Despite promising results in using the modified Clauser method to estimate  $U_\tau$ ,  $\epsilon$ , and  $\Delta U^+$ , the combination of mentioned challenges above have raised questions about the accuracy of the outcomes [74]. Therefore, a second technique that relies on the outer-layer similarity hypothesis [40] to “improve” the estimation is introduced [2,73]. An improvement to estimate  $U_\tau$  was made by fitting the rough-wall defect profile ( $U_\infty^+ - U^+$  vs  $y^*/\delta_{99}$ ) onto the smooth-wall data from the outer region  $y^*/\delta_{99} \approx 0.1$ , which refers to velocity defect method. Note that it is difficult to determine *a priori* whether a flow would obey the outer-layer similarity hypothesis or not, particularly for 2D roughness that are known to exhibit various different outcomes. The authors are also aware that it is not immediately clear if either of these methods will be applicable for 2D roughness where some reports have indicated that such roughness can alter flow dynamics far into the outer region. Hence it may raise questions about the efficacy in relying on the outer-layer similarity hypothesis to improve the  $U_\tau$  and  $\Delta U^+$  estimation. Jiménez [10] suggested that when  $\delta_{99}/k > 40$ , the roughness effect can not extend to the outer flow. Note that for most k-type roughness results with  $4 \leq p/k \leq$



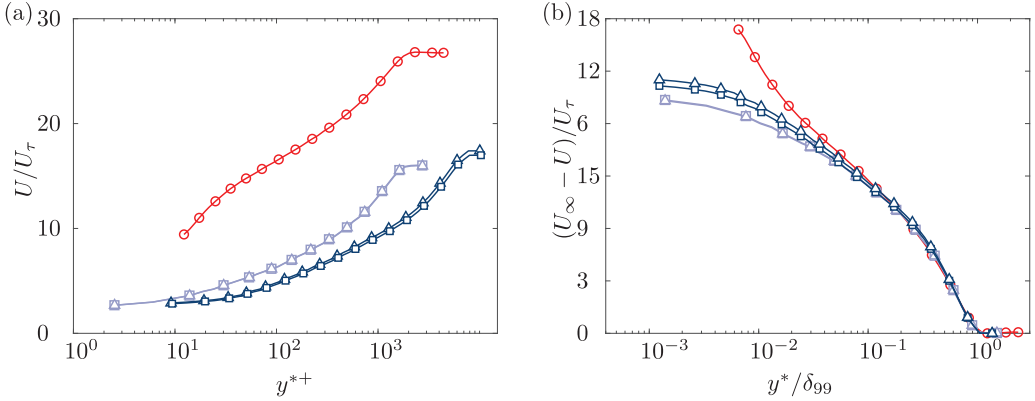


FIG. 3. Comparison in estimating  $U_\tau$  and  $\Delta U^+$  of the 2D rough-wall case at  $\text{Re}_\tau = 1840$  (pk8A, light purple) and  $\text{Re}_\tau = 7500$  (pk8E, dark blue) using the modified Clauser method (open triangle symbol) and the “improved” technique of Monty *et al.* [73] (open square symbol). For completion, the smooth-wall case at  $\text{Re}_\tau = 1900$  is also plotted (red line with open circle). Mean velocity profiles (a) and mean velocity defect (b).

48, the ratios of  $\delta_{99}/k$  are larger than 40, as per Tables I and II. These rough-wall cases satisfy the criterion of Jiménez [10], which implies the validity of the outer-layer similarity. For the d-type roughness ( $p/k < 4$ ), Perry *et al.* [28] originally reported the collapse between Hama’s reference equation [7] and the rough-wall data in the form of the velocity defect law. Smalley *et al.* [78] and Mochizuki *et al.* [79] consequently confirmed that the outer layer similarity is observed in the mean velocity and turbulence intensity profiles at friction Reynolds numbers up to  $\text{Re}_\tau \approx 2000$ . Hence, the technique can provide an acceptable estimation for the friction velocity over the rough surfaces. Figure 3 shows the comparison of the mean velocity and defect profiles from the 2D rough-wall cases at the lowest and highest friction Reynolds number cases using the modified Clauser method and the improved technique of Monty *et al.* [73]. The plot shows an excellent collapse for the lowest friction Reynolds number results, with differences less than 1% in terms of  $U_\tau$  and  $\Delta U^+$ . The highest friction Reynolds number results also show small differences for both parameters of about 2.5%. These differences are well within the expected error as indicated by Flack *et al.* [74] and Schultz and Myers [75]. The technique is believed to improve the uncertainty of  $U_\tau$  estimated from the modified Clauser method, the uncertainty of this technique should be within 3%–5%. Therefore, the improved estimation technique, a combination of modified Clauser method used to obtain  $\epsilon$  and velocity defect method used to obtain  $U_\tau$  and  $\Delta U^+$ , was used for all rough-wall data in this report.

After the roughness function  $\Delta U^+$  is determined, the equivalent sand grain roughness,  $K_s$ , is calculated as per equation [17], such that

$$\Delta U^+ = \frac{1}{\kappa} \ln(K_s^+) + B - 8.5. \quad (2)$$

For the cases of the matched pitch ratio measurements ( $p/k = 8$ ), the data from the highest friction Reynolds numbers case were used to compute  $K_s$  with Eq. (2) as these rough-wall data are apparently fully rough at friction Reynolds number  $\text{Re}_\tau \approx 7500$  and  $\Delta U^+ = 12.54$  [17]. The ratio of  $\delta_{99}/K_s$  was determined with a constant  $K_s$  and various  $\delta_{99}$  and summarized in Table I. For the other rough walls ( $p/k = 2-4, 12-128$ ), all data were assumed to be fully rough and  $K_s$  was computed using Eq. 2. All rough-wall data are plotted in Fig. 4. Note that the rough-wall cases of  $p/k = 2, 96$  and 128 with  $\Delta U^+ < 8$  appear to be in the transitionally rough regime but are close to the fully rough regime. These cases estimate  $K_s^+$  within 6% uncertainty, assuming the fully rough regime.

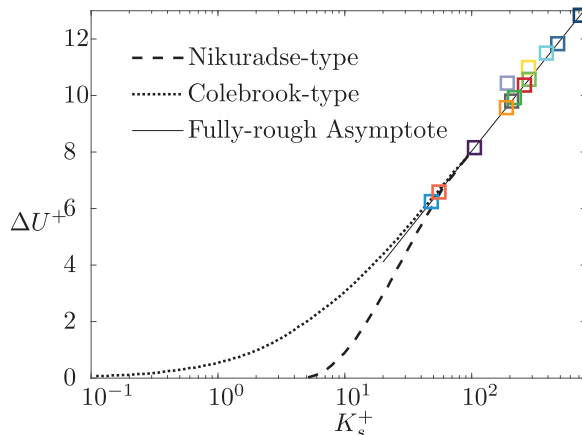


FIG. 4. The roughness function,  $\Delta U^+$  versus the inner-scaled equivalent sand-grain roughness height,  $K_s^+$ . The square symbols are the present results as per Tables I and II.

### III. MATCHED PITCH RATIO COMPARISONS

#### A. Turbulence statistics

Figure 5 shows the time-averaged statistics for the 2D rough wall with a pitch ratio  $p/k = 8$ , friction Reynolds numbers in the range  $\text{Re}_\tau = 1840\text{--}7500$  and  $\delta_{99}/k = 49\text{--}54$  (open symbols as defined in Table I). The rough-wall data are compared with those of the smooth wall at  $\text{Re}_\tau = 1900$ , 4300, and 8400, where the two highest  $\text{Re}_\tau$  cases are taken from Marusic *et al.* [80]. Figure 5(a) shows inner-scaled mean velocity profiles, which clearly indicate the downward shift for the rough-wall TBLs relative to those of the smooth wall. The downward shift is quantified by  $\Delta U^+$ , such that the mean velocity equation in the logarithmic layer for a rough wall is

$$U^+ = \frac{1}{\kappa} \ln \frac{(y - \epsilon) U_\tau}{\nu} + B - \Delta U^+. \quad (3)$$

The  $\Delta U^+$  values are given in Table I. The downward shift increases with increasing  $\text{Re}_\tau$ , which is a typical behavior for fully developed rough-wall TBLs [20].

Figure 5(b) shows the inner-scaled turbulence intensity. The smooth-wall reference cases indicate a near-wall peak at  $y^{*+} \approx 15$ , due to the highly energetic near-wall cycle of streaks and quasistreamwise vortices [81]. For the lowest friction Reynolds number ( $\text{Re}_\tau = 1900$ ), the near-wall peak is lower than those of the higher friction Reynolds numbers ( $\text{Re}_\tau = 4300$  and 8400), which indicates that the near-wall peak of the normalized turbulence intensity shows  $\text{Re}_\tau$  dependence. This finding has been previously reported by Marusic *et al.* [80] and Squire *et al.* [77]. For the rough-wall TBLs, as expected, the normalized turbulence intensity at the near-wall region ( $y^{*+} < 30$ ) is reduced, compared with the smooth-wall results, which is generally attributed to the disturbance of the near-wall cycle of streaks and quasistreamwise vortices near the surface roughness [73,77,82,83]. In addition, the magnitude of the near-wall normalized turbulence intensity for the rough-wall cases reduces with increasing  $\text{Re}_\tau$ , which is expected for rough-wall TBLs [20,83]. Squire *et al.* [20] and Djenidi *et al.* [83] reported that the reduction is associated with the disturbance of the near-wall cycle and the corresponding increase of  $U_\tau$  due to the disturbance caused by the roughness elements. Note that the present results contain hot-wire spatial attenuation, particularly at high  $\text{Re}_\tau$ , where the  $l^+$  value reaches 47.8 at  $\text{Re}_\tau = 7500$ . Also, the reduction of the near-wall turbulence intensity is associated with increasing roughness Reynolds numbers, from  $k^+ = 37$  at the lowest  $\text{Re}_\tau$  to  $k^+ = 140$  at the highest  $\text{Re}_\tau$ , which has been reported in the DNS pipe flow study of Chan *et al.*

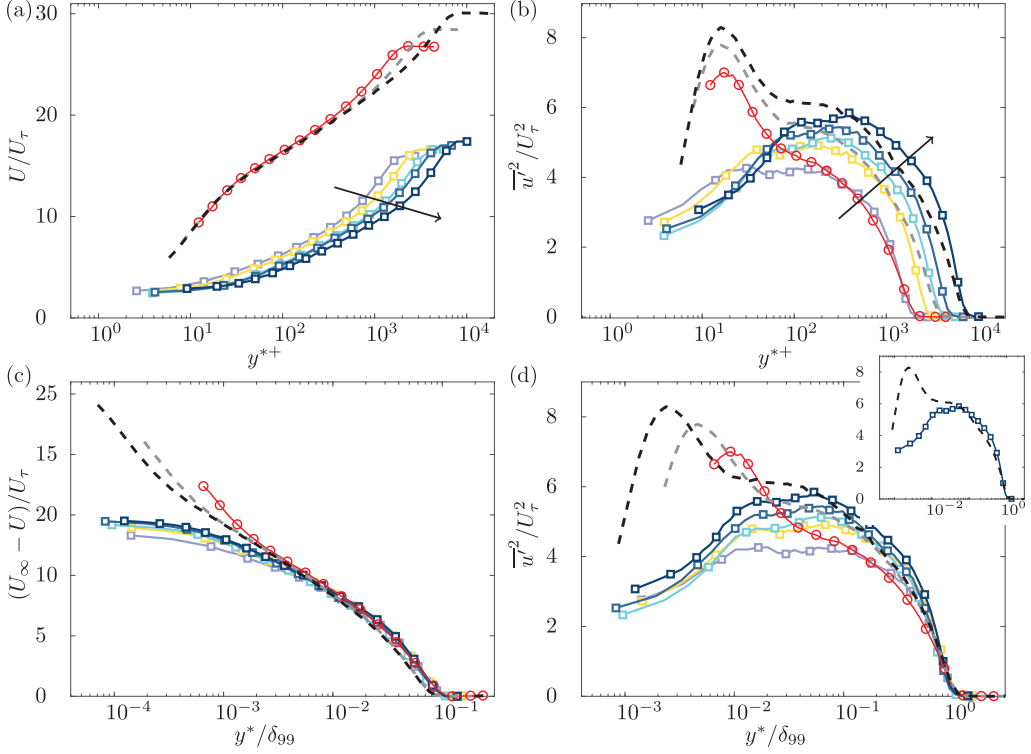


FIG. 5. Comparison of the 2D roughness with  $p/k = 8$  ranging from  $\text{Re}_\tau = 1840\text{--}7500$  (refer color codes to Table I) and the smooth-wall TBLs at  $\text{Re}_\tau = 1900$  (red line with open circle) and two higher friction Reynolds number cases from the literature,  $\text{Re}_\tau = 4300$  (gray dash line) and  $\text{Re}_\tau = 8400$  (black dash line) [80]. The black arrow indicates the increases of  $\text{Re}_\tau$ . Mean velocity profiles (a); inner-scaled turbulence intensity profiles (b); mean velocity defect profiles (c); and outer-scaled turbulence intensity profiles (d).

[15]. Farther from the wall, there is an increase of turbulence intensity with  $\text{Re}_\tau$ , particularly in the logarithmic region, which is a typical behavior for both smooth and rough walls [20,80].

Figures 5(c) and 5(d) show the velocity deficit and the outer-scaled turbulence intensity profiles. The velocity deficit profiles show good agreement between the rough- and smooth-wall results, particularly from  $y^*/\delta_{99} \approx 0.03$ . The collapse indicates that the assumption of the outer-layer similarity in the form of the velocity defect is appropriate. For the normalized turbulence intensity profiles [Fig. 5(d)], the rough-wall results merge beyond  $y^*/\delta_{99} = 0.5$ , such that the maximum difference at this location is 13% ( $\approx 0.4$ ), which is similar to the spread for the sand-grain roughness experiment of Squire *et al.* [77] and the circular rod roughness experiment of Djenidi *et al.* [83]. In Fig. 5(d) all rough-wall data start to merge with the smooth-wall data at  $y^*/\delta_{99} \approx 0.5$ . However, the deviation between the smooth- and rough-wall data at this location still spans a range,  $\bar{u}'^2|_{\text{rough}} - \bar{u}'^2|_{\text{smooth}} \approx 0.46$  (16%), which is larger than the uncertainty range of  $U_\tau^2$ . According to the outer layer similarity hypothesis, the roughness effect is confined to the roughness sublayer ( $y^* < \max\{5k, 3K_s\}$ ) [74]. For the rough-wall results,  $K_s > 5k$ , so that the roughness sublayers should be  $y^* \leq 3K_s$ , which are  $y^*/\delta_{99} \leq 0.45$ . All rough-wall results are observed to collapse with the smooth-wall cases at  $y^*/\delta_{99} \approx 0.7$  in Fig. 5(d), with a small discrepancy of  $\approx 6\%$  ( $\bar{u}'^2|_{\text{rough}} - \bar{u}'^2|_{\text{smooth}} \approx 0.1$ ). The location is above the defined roughness sublayers ( $y^*/\delta_{99} > 0.45$ ). The inset in Fig. 5(d) shows the comparison between the highest  $\text{Re}_\tau$  cases of the smooth and rough wall. The difference at  $y^*/\delta_{99} = 0.5$  is  $\bar{u}'^2|_{\text{rough}} - \bar{u}'^2|_{\text{smooth}} \approx 0.46$  (16%), which is also observed in the 2D circular rod

roughness study by Djenidi *et al.* [83]. This result may be caused by the relatively low ratio of  $\delta_{99}/k = 49\text{--}53.9$ , even though the present study is conducted at a relatively high  $\text{Re}_\tau$ . A contrary result is observed in the experimental study by Efros and Krogstad [46] over a similar 2D roughness with  $\delta_{99}/k \geq 96$  at friction Reynolds numbers  $\text{Re}_\tau \geq 9900$ , which reported, for the normalized turbulence intensity profiles, that excellent collapse between the rough- and smooth-wall results start from  $y^*/\delta_{99} = 0.05$ , with a discrepancy of  $\approx 2\%$ . The present rough-wall results show similarity in terms of the normalized turbulence intensity, with a small difference of 6% from  $y^*/\delta_{99} = 0.7$ . Hence, the present result and the literature from Efros and Krogstad [46] strengthen the notion that 2D roughness can show more convincing support for the outer-layer similarity hypothesis when the scale separation ratio  $\delta_{99}/k$  is higher ( $\delta_{99}/k \geq 100$ ) in a higher Reynolds number environment ( $\text{Re}_\tau \geq 10\,000$ ).

### B. Comparisons of drag coefficient $C_f$

The drag coefficient  $C_f$  is defined as

$$C_f = \frac{2\tau_w}{\rho U_\infty^2} = \frac{2U_\tau^2}{U_\infty^2}. \quad (4)$$

In Fig. 6 the drag coefficients of the rough-wall TBLs in Table II are compared with the five TBL studies from Lee and Sung [34], Nadeem *et al.* [35], Lee *et al.* [39], Choi *et al.* [47], and Efros and Krogstad [46], which are for similar 2D roughness with  $p/k = 8$ , and covering both DNS and experiments. For the low friction Reynolds number range, the drag coefficient increases with increasing  $\text{Re}_\tau$ , from 0.0043 at  $\text{Re}_\tau = 360$  and reaches its maximum at 0.012 at  $\text{Re}_\tau = 570$  [Fig. 6(a), black stars]. For higher  $\text{Re}_\tau$ , the drag coefficient reduces with increasing  $\text{Re}_\tau$  before becoming approximately constant when  $\text{Re}_\tau \geq 3900$ . In Fig. 6(b) there are two trends of  $C_f$ , which reduce with increases of  $\delta_{99}/k$ , but reach two constant values at 0.0068 ( $\text{Re}_\tau \geq 570$ ) and 0.0043 ( $\text{Re}_\tau \leq 570$ , black stars), respectively.

Figures 6(c) and 6(d) show how  $C_f$  varies with the normalized equivalent roughness  $K_s^+$  and the roughness function  $\Delta U^+$ . The three low- $\text{Re}_\tau$  results, for which with  $C_f < 0.008$  (black star), have  $K_s^+ < 70$  and  $\Delta U^+ < 8.5$  (indicated by the vertical dash lines). Nikuradse [17] classified that surfaces are hydraulically smooth for  $K_s^+ < 5$ ; transitionally rough for  $K_s^+ < 70$  and fully rough for  $K_s^+ \geq 70$ . Also, the fully rough cases are well documented as having  $\Delta U^+ \geq 8.5$  [10,17,84,85]. Hence, these three data sets are hydraulically smooth and transitionally rough cases, which are excluded from the following discussion.

For the data having  $\Delta U^+ \geq 8.5$ , Figs. 6(a) and 6(b) show that the drag coefficient  $C_f$  reduces from 0.012 at  $\text{Re}_\tau = 570$  and achieves a constant of  $C_f \approx 0.0069$  when  $\text{Re}_\tau \geq 3900$  and  $\delta_{99}/k \geq 50$ . Note that, based on Eq. (4), the convergence of  $C_f$  indicates the entire mean velocity profile shifts horizontally to larger  $y^{*+}$ , as shown in Fig. 5(a). The trend of the drag coefficient approaching a constant is consistent with that of sand-grain or k-type roughness as suggested by Flack *et al.* [86]. Djenidi *et al.* [83] suggested that  $C_f$  converges to 0.0071 when  $\text{Re}_\tau > 4000$  over a circular-rod 2D roughness, but the present results bring up the importance of the scale separation  $\delta_{99}/k$  and  $k^+$ , where we suggest  $\delta_{99}/k > 50$  and  $k^+ > 75$  to achieve the fully rough regime with a constant  $C_f$  for 2D roughness k-type roughness. For fully rough 2D roughness TBLs at sufficiently high  $\text{Re}_\tau$  and  $\delta_{99}/k$ , the similar magnitudes of converging  $C_f$  over 2D roughness with different cross-sectional shapes indicate the drag coefficient for the rough-wall TBL is independent of the shape of the cross section.

### C. Spectra analysis

Figure 7 shows the energy spectra maps for the rough-wall cases in Table I and the smooth-wall case at  $\text{Re}_\tau = 1900$ . The energy spectra are the power spectral density of streamwise velocity fluctuations,  $\Phi_{uu}$ , premultiplied by the streamwise wave number,  $k_x$ . The spatial structure of

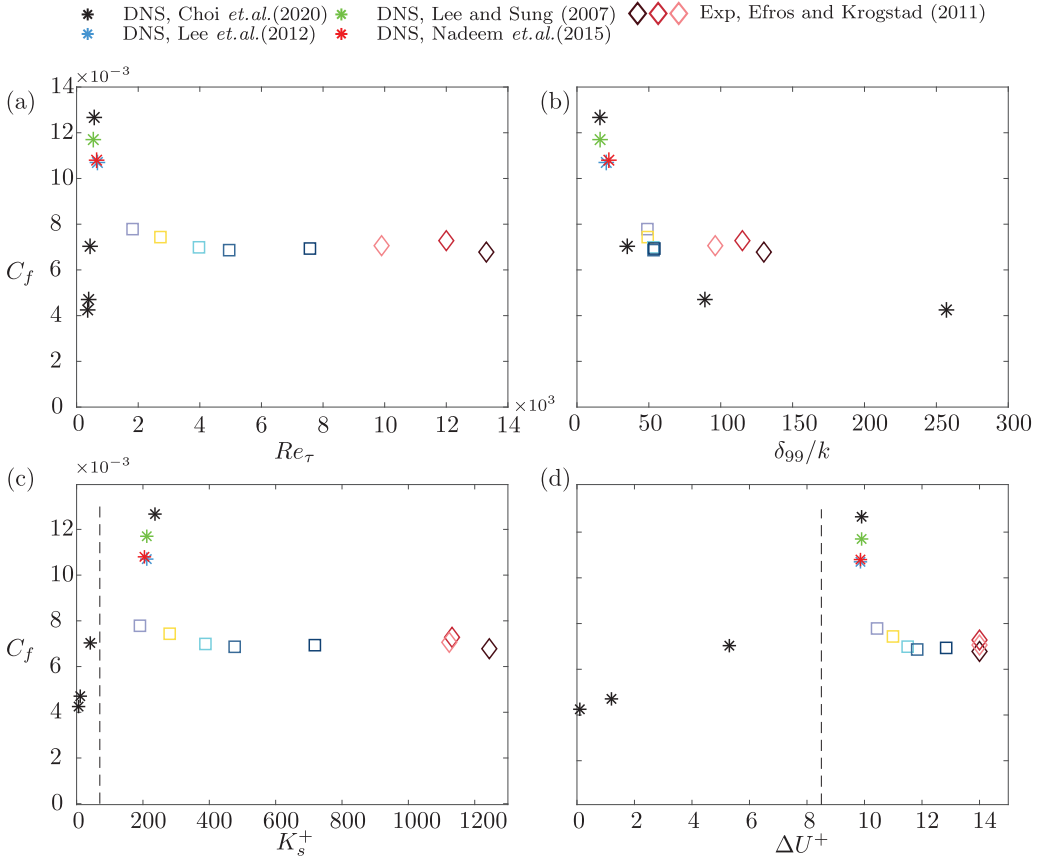


FIG. 6. The variations of  $C_f$  on  $Re_\tau$  (a),  $\delta_{99}/k$  (b),  $K_s^+$  (c) and  $\Delta U^+$  (d) from the literature and the present data of  $p/k = 8$ . The symbols of star with different colors are the square-bar roughness DNS studies [34,35,39,47]. The diamonds in light red to dark red are the experimental roughness TBL study at  $Re_\tau = 9900$ –13000 [46]. The square symbols are the present results as per Table I.

streamwise velocity fluctuations is deduced from temporally sampled point measurements using Taylor’s hypothesis [87]. The streamwise wave number is defined as  $k_x = 2\pi f/U_c$ , where  $f$  is the frequency and  $U_c$  is the convection velocity, which is assumed to be equal to the local mean streamwise velocity [73]. All spectra are scaled by the friction velocity,  $U_\tau$ , and plotted against the normalized streamwise wavelength,  $\lambda_x^+ = (2\pi/k_x)/(v/U_\tau)$ .

Figure 7(a) shows the energy spectra for the smooth-wall TBL. The smooth-wall spectra map has a highly energetic peak near the wall at  $y^{*+} \approx 15$  and  $\lambda_x^+ \approx 1000$ , commonly termed the “inner peak,” which indicates the energy signature from the near-wall cycle of streaks and quasistreamwise vortices [63,88]. At sufficiently high friction Reynolds number, a second peak with a larger wavelength ( $\lambda_x/\delta_{99} \approx 6$ ) can be observed at the wall normal location of  $y^*/\delta_{99} \approx 0.06$  (the midpoint of the logarithmic region) [89]. The second peak is known as the “outer peak” and indicates superstructure events [63]. Because the friction Reynolds number for the smooth wall in this plot is relatively low ( $Re_\tau = 1900$ ), only the beginning of an outer peak that can be observed.

For the rough-wall spectra at a similar friction Reynolds number [Fig. 7(b); pk8A], the inner peak has a smaller magnitude than the smooth-wall inner peak, which results in the reduction of the normalized turbulence intensity in the near-wall region at  $y^{*+} \approx 15$  [Fig. 5(b)]. Figure 7(b) also shows that the larger-scale flow structures ( $\lambda_x^+ > 1000$ ) in the near-wall region contain lower normalized

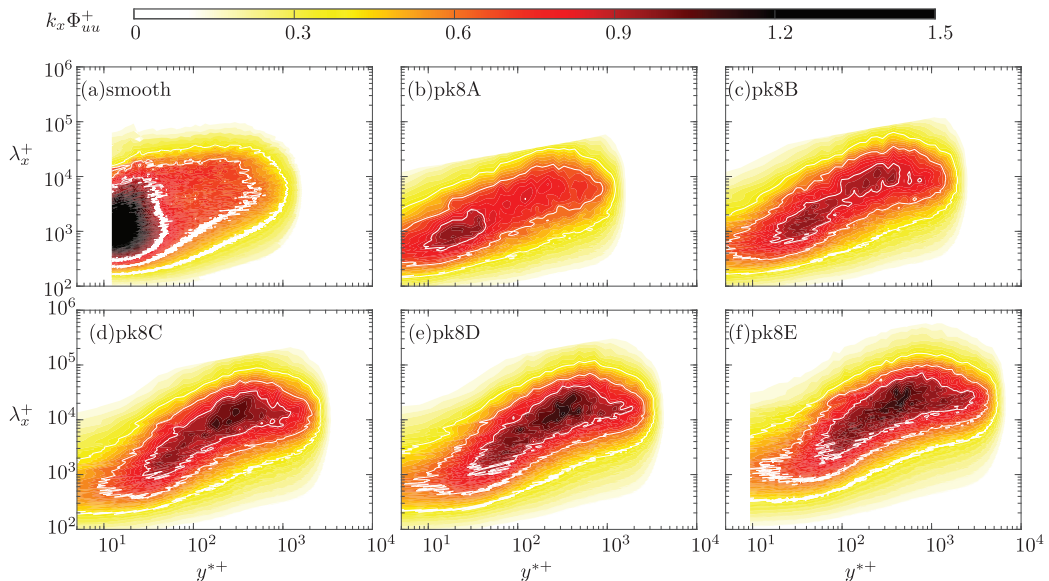


FIG. 7. Premultiplied spectra contour profiles for the smooth wall at  $Re_\tau = 1900$  (a) and 2D roughness with  $p/k = 8$  ranging from  $Re_\tau = 1840$ – $7500$  for (b)–(f). The white isolines correspond to the rough- and smooth-wall case with  $k_x \Phi_{uu}^+ = 0.5, 0.8,$  and  $1.1$ .

energy due to roughness. In contrast, the case of pk8A has a more pronounced outer peak, and its energy spectra extends farther from the wall than that of the smooth-wall case. Again, this outer-peak behavior is also expected based on the vertical shift of the rough-wall case’s turbulence intensity, particularly in the outer region. Hence, there are more highly energetic large-scale activities in the outer region ( $y^{*+} > 400$ ) for the 2D roughness flows than the smooth-wall flow at a similar friction Reynolds number. Figures 7(b)–7(f) show that as the friction Reynolds number increases for the rough wall the inner peak decreases and the outer peak increases. Therefore, the large-scale motions dominate the TBL for the 2D roughness at moderate  $Re_\tau$ . Monty *et al.* [73] and Squire *et al.* [77] report similar observations for TBLs above braille-type roughness and sand-grain/k-type roughness, respectively.

In Fig. 8 the energy spectral density,  $k_x \Phi_{uu}^+$ , are compared at different wall-normal positions. Figure 8(a) shows the spectrum comparisons at the inner coordinate location of  $y^{*+} \approx 15$  (where the inner peak is located) to investigate the energy distribution of the near-wall structures. At similar  $Re_\tau$ , the rough-wall result of pk8A has a lower normalized energy spectrum than that of the smooth wall. The reduction of the normalized energy is similar in magnitude, but the reduction ratios are approximately 30% and 55% for the near-wall cycle structures ( $\lambda_x^+ \approx 1000$ ) and the larger-scale structures ( $\lambda_x^+ \approx 6000$ ), respectively. Compared with the smooth-wall result, the energy contribution for the rough-wall result is shifted from the larger-scale structures to the smaller-scale ones at this relatively low Reynolds number. For the rough-wall data at varying Reynolds numbers, the normalized spectra collapse well for larger-scale structures ( $\lambda_x^+ \geq 2000$ ). The smaller-scale motions experience a reduction of the energy contribution with increasing Reynolds numbers up to  $Re_\tau \approx 3900$ , as indicated by the arrow. Note that the hot-wire spatial resolution reduces with increasing  $Re_\tau$  as the  $l^+$ -value increases from 13 to 25, where the maximum  $l^+$  is slightly higher than the suggestion of  $l^+ < 20$  [66]. This observation indicates that the energy distribution from the smaller-scale motions reduces with increasing Reynolds numbers up to  $Re_\tau \approx 3900$  and this reduction is associated with the combination of the insufficient hot-wire resolution and the disturbance of the near-wall cycle.

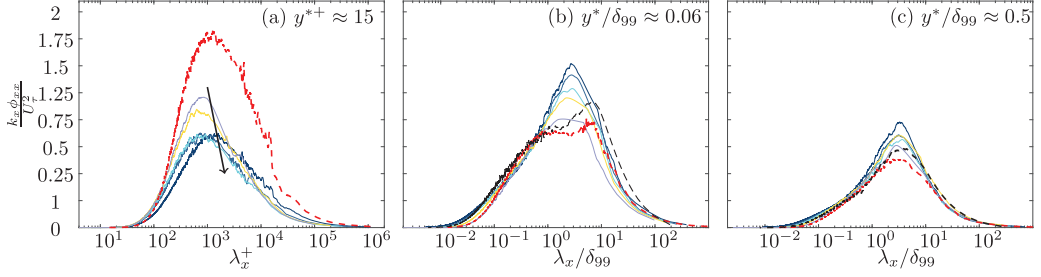


FIG. 8. Premultiplied spectra profiles in streamwise direction for  $p/k = 8$  at different wall-normal locations, the near-wall region at  $y^{*+} \approx 15$  (a) in inner-scaled coordinate and the log region at  $y^*/\delta_{99} \approx 0.06$  (b), and the wake region region at  $y^*/\delta_{99} \approx 0.5$  (c) in outer-scaled coordinate. Red and black dash lines are the smooth-wall results at  $Re_\tau = 1900$  and  $3500$ , respectively, where the higher friction Reynolds number data refer to Örlü *et al.* [90]. Arrow indicates the increases of Reynolds number. The color code for all rough-wall cases are the same as per Table I without square markers.

Figures 8(b) and 8(c) show spectrum comparisons at two outer coordinate locations,  $y^*/\delta_{99} = 0.06$  and  $0.5$ , which correspond to the midpoints of the log and the wake regions, respectively. In the log region [Fig. 8(b)], the rough-wall cases with the three highest friction Reynolds numbers (pk8C–E) collapse over the entire range of wavelengths. The collapse for the highest friction Reynolds numbers is consistent with the approximately constant value of  $C_f$  at these  $Re_\tau$ , and supports the notion that the 2D rough-wall TBL becomes fully rough when  $Re_\tau \geq 3900$ . For the rough-wall spectrum at a low friction Reynolds number (pk8A), the spectrum peak is slightly higher than the smooth-wall profile at a similar friction Reynolds number. The highly energetic activities are associated with the very large-scale motions (VLSMs) or superstructures with the length scale of  $3\delta_{99} - 6\delta_{99}$  [63,91]. For comparison at a higher friction Reynolds number  $Re_\tau \approx 3500$ , the discrepancy between the smooth- and rough-wall spectra at that wavelength range becomes larger. The discrepancy change between the two Reynolds numbers indicates that the VLSMs become more energetic with increasing  $Re_\tau$  for 2D square-bar roughness in the log region, compared with the smooth-wall data at corresponding Reynolds numbers.

Figure 8(c) shows five rough-wall spectra collapsing with each other in the wake region at  $y^*/\delta_{99} \approx 0.5$ . Compared with the smooth-wall results, all the rough-wall results show a good agreement at the wavelength range of  $\lambda_x/\delta_{99} > 10$ , with a small difference of  $\approx 10\%$ . However, the rough-wall results show a greater peak in shape for the interval range of  $0.5 \leq \lambda_x/\delta_{99} \leq 10$ , with an increase of  $\approx 26\%$ , compared with the smooth-wall profile. This result reflects the higher normalized turbulence intensity observed in Fig. 5(d) and supports the conclusion that the roughness effect on increasing normalized turbulence intensity extends to the wake region at  $y^*/\delta_{99} \approx 0.5$ .

As the friction Reynolds number increases, in general, the normalized energy reduction induced by the roughness becomes more significant for the smaller-scale structures ( $\lambda_x^+ \leq 2000$ ) in the near-wall and the VLSMs become more energetic in the log region. The roughness introduces more normalized energy to most turbulent eddies in the wake region, which seems to be independent of friction Reynolds numbers.

#### D. Autocorrelation analysis

Figure 9 shows the autocorrelation of the streamwise velocity fluctuation,  $R_{uu}$ , at three wall-normal locations as per Fig. 8. The autocorrelation at the reference wall-normal location  $y_{\text{ref}}$  is defined as

$$R_{uu}(\Delta x, y_{\text{ref}}) = \frac{\overline{u(x, y_{\text{ref}})u(x + \Delta x, y_{\text{ref}})}}{\sigma_u \sigma_u}, \quad (5)$$

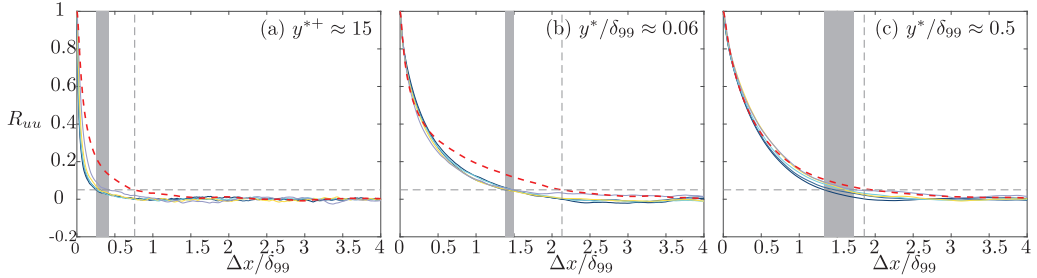


FIG. 9. Autocorrelation of the streamwise velocity fluctuation  $R_{uu}$  for the smooth wall at  $Re_\tau = 1900$  and 2D roughness with  $p/k = 8$  ranging from  $Re_\tau = 1840$  to  $7500$  in the near-wall region at  $y^{*+} \approx 15$ (a), the log region at  $y^*/\delta_{99} \approx 0.06$ (b) and the wake region at  $y^*/\delta_{99} \approx 0.5$ (c). The horizontal dash line denotes  $R_{uu} = 0.05$ , and the vertical dash line indicates the average size of turbulent structures for the smooth-wall result. The sizes for all rough-wall cases are located within the gray shaded band. The color code for all rough-wall cases are the same as per Table I without square markers.

where  $u$  is the spatial quantities of the streamwise velocity separated in the streamwise directions by the distance  $\Delta x$ , which is transformed from the time-series signals with single point measurements by using Taylor's hypothesis [87]. Here,  $\sigma$  is a standard deviation and the overline indicates the spatial average. In Fig. 9 the streamwise distance  $\Delta x/\delta_{99}$  at the zero crossing of  $R_{uu} = 0.05$  reflects the average turbulence structures length scale feature to a certain extent [92], which is emphasized by the vertical dash lines and the shaded bands for the smooth- and rough-wall results, respectively, where the average length scale for all rough-wall data is summarized in the shaded band for brevity. Figure 9(a) shows that the rough-wall profiles are generally lower than that of the smooth wall in the near-wall region, and the scale reduction indicated by the vertical line and band reaches 50% ( $\Delta x/\delta_{99}|_{\text{smooth}} - \Delta x/\delta_{99}|_{\text{rough}} \approx 0.35$ ). This observation is consistent with the reduction of energy distribution on the larger-scale structures shown in Fig. 8(a), which indicates the near-wall streamwise extents are much shorter than the smooth-wall TBL. This is caused by disturbance of regularly distributed roughness elements, which is also reported in other 2D roughness studies [33,39].

Figures 9(b) and 9(c) show autocorrelation results at two wall-normal positions in outer-scaled coordinate, corresponding to the midpoints of the log and wake regions. In Fig. 9(b), the rough-wall profiles agree well with each other and they are still slightly lower than that of the smooth wall. This observation indicates the reduction of the average length scale of turbulent structures caused by 2D roughness occurs in the log region. However, this effect is independent of friction Reynolds numbers, which is consistent with the similar shapes of spectrum profiles for five rough-wall results in Fig. 8(b). In the wake region [Fig. 9(c)], all rough-wall profiles are close to collapsing with the smooth-wall profile, which supports the outer-layer similarity hypothesis in the length scale of the streamwise structures from  $y^*/\delta_{99} = 0.5$ . For Reynolds number influences, the collapse of five rough-wall profiles at three wall-normal locations implies that the average length scale of turbulent structures is insensitive to friction Reynolds numbers may be related to roughness geometries.

#### IV. MATCHED REYNOLDS NUMBER COMPARISON

Section III analyzed the Reynolds number effects on the classic 2D k-type roughness with  $p/k = 8$ . Apart from the Reynolds number effects, the pitch ratio  $p/k$  is another key parameter influencing the mean statistics and turbulent structures of 2D roughness TBLs. This section will present the rough-wall results with a range of  $p/k = 2-128$  at a similar friction Reynolds number  $Re_\tau \approx 3500$ . The rough-wall parameters are listed in Table II.



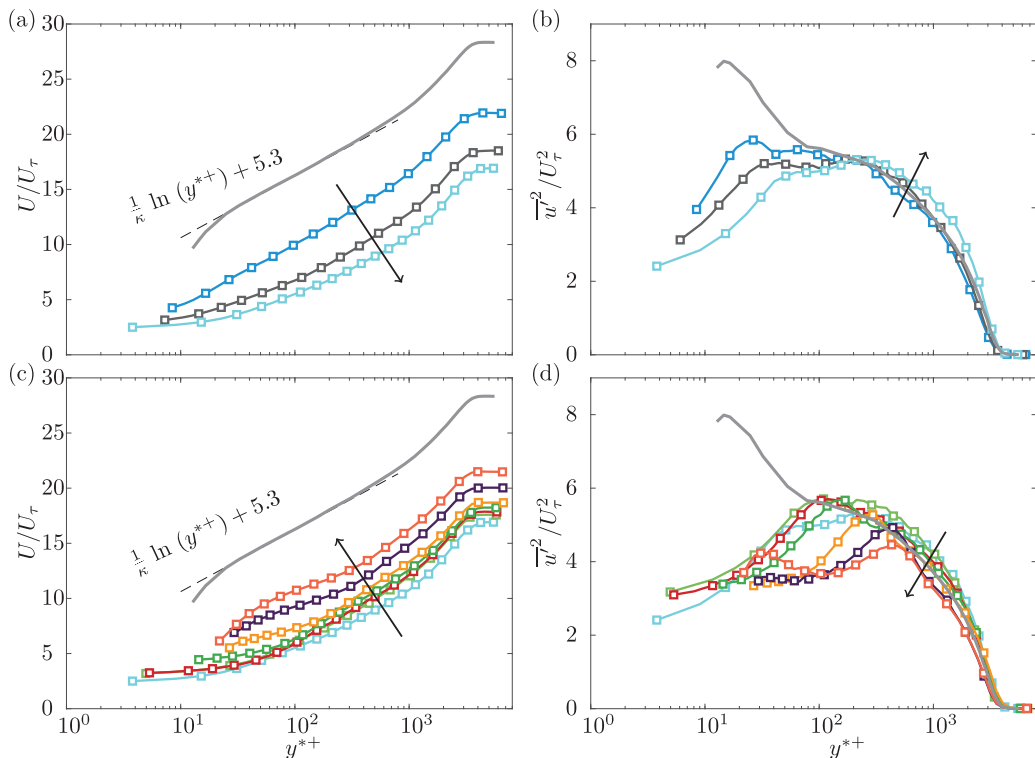


FIG. 10. Comparison of the 2D roughness with  $p/k = 2$  to 128 at  $Re_\tau \approx 3500$  (refer color codes to Table II) and the smooth-wall TBL from the literature,  $Re_\tau = 3500$  (gray solid line) from Örlü *et al.* [90]. Mean velocity profiles for  $p/k \leq 8$  (a) and  $p/k \geq 8$  (c); inner-scaled turbulence intensity profile for  $p/k \leq 8$  (b) and  $p/k \geq 8$  (d).

### A. Turbulence statistics

In Fig. 10 the inner-scaled mean velocity profiles [Figs. 10(a) and 10(c)] and turbulence intensities [Fig. 10(b) and 10(d)] for rough walls with various pitch ratios ( $p/k = 2$ –128) are plotted along with the smooth-wall result of Örlü *et al.* [90] for matching at  $Re_\tau \approx 3500$ . The top row [Figs. 10(a) and 10(b)] shows the cases with  $p/k = 2, 4$ , and 8, and the lower row [Figs. 10(c) and 10(d)] shows the cases  $p/k = 8, 12, 16, 24, 48, 96$ , and 128.

Figure 10(a) shows an increase of  $\Delta U^+$  (the downward shift in the mean velocity profiles) as  $p/k$  increases until  $p/k = 8$ , which is similar with the experiment and CFD results of Furuya *et al.* [23], Leonardi *et al.* [38], and Lee *et al.* [39]. Such behavior is consistent with sand-grain/ $k$ -type roughness, where the mean velocity profiles shift further downwards when a surface becomes rougher (higher  $K_s$ ). For  $p/k \geq 8$  [Fig. 10(c)], the mean velocity profiles of the rough-wall cases shift up as  $p/k$  increases ( $\Delta U^+$  becomes lower with increasing  $p/k$ ). This observation indicates that the roughness blockage effect reduces, and the flow appears to be transitioning to a smooth-wall TBL, which is also observed in the DNS study of Nadeem *et al.* [35].

The normalized turbulence intensity [Fig. 10(b)] shows that the near-wall peaks (at  $y^{*+} \approx 15$ ) are lower than the smooth-wall case and the amplitude decreases as the pitch ratio increases, indicating the disturbance or suppression of the near-wall cycle of streaks and quasistreamwise vortices around the surface roughness. In addition, the wall-normal location of the inner peak shifting towards the outer region and the amplitude decreasing with the increases of  $p/k$  is consistent with the behavior of streamwise normal stresses in the DNS study at  $Re_\tau \approx 600$  by Lee *et al.* [39]. Since the present

results are performed at higher friction Reynolds numbers ( $Re_\tau \approx 3500$ ), more pronounced outer-layer peaks are observed for the rough-wall cases of  $p/k = 4$  and  $8$  compared to the result of Lee *et al.* [39]. In the log region, the outer-layer peak increases with  $p/k$ , indicating that there are more turbulent activities or stronger turbulent motions farther from the wall with increasing  $p/k$  (at least until  $p/k = 8$ ). This behavior is also consistent with sand-grain/ $k$ -type roughness (the rougher surface induces higher normalized turbulence intensity in the outer region).

Figure 10(d) shows that the inner-scaled turbulence intensities for  $p/k \geq 8$  are significantly lower than that of the smooth-wall case, which may be due to the damping or disturbance of the near-wall cycle of streaks and vortices by the roughness. At the near-wall region, the turbulence intensities for  $p/k = 8-24$  are similar, making it difficult to correlate the magnitude of the turbulence intensity with the pitch ratio effect. However, the near-wall turbulence intensities for  $p/k > 24$  at  $y^{*+} = 40-100$  are much lower than the other rough-wall results. An uptrend and a near-wall peak are captured for the rough-wall cases of  $p/k = 96$  and  $128$  at  $y^{*+} \approx 40$ , respectively. This result indicates the near-wall flow is transitioning back to that of the smooth-wall TBL when  $p/k \geq 96$ . A similar trend is observed in the DNS result by Nadeem *et al.* [35], who reported that the near-wall peak emerges and increases from  $p/k = 32-128$ . The magnitude of the near-wall peak for  $p/k = 128$  in the DNS result ( $Re_\tau \approx 600$ ) is  $\overline{u}^2/U_\tau^2 = 5.2$  [35], and the corresponding value in the present result is  $\overline{u}^2/U_\tau^2 = 4.2$  for the higher  $Re_\tau$  TBL. As expected, the peak reduction is partially caused by the low hot-wire spatial resolution ( $l^+ = 36.6$ ). However, the reduction caused by the spatial resolution effect should be less than 10% for  $Re_\tau \geq 3500$  [66]. The peak reduction reaching nearly 20% is also associated with the Reynolds number influence, which indicates that the forming rate of the near-wall structures is slower at higher  $Re_\tau$  for large  $p/k$ .

In the log region ( $y^{*+} = 200 \leq y^{*+} \leq 700$ ), Fig. 10(d) shows that the normalized turbulence intensity reduces with increasing  $p/k$  from  $p/k = 24-128$ . In addition, the outer-layer peak reduces in magnitude, and the wall-normal position where it occurs shifts towards the outer region with increasing  $p/k$ . The reducing peaks may be related to the flow relaxation in the TBL over a backward-facing step (BFS) because the flow traveling over each square-bar element for rough walls with large  $p/k$  is similar to the flow over a BFS. The flow relaxation is a well-known behavior downstream of the flow reattachment after a BFS, where the turbulence intensity is lower than their fully developed value in the log region of the smooth-wall TBL [93,94]. A recent numerical study by Ding and Smits [95] about the BFS flows presented the turbulence intensity profiles at different downstream locations and observed a similar behavior of the outer-layer peaks, as shown in Fig. 10(d). However, it remains unknown how the decreasing outer-layer peak is related to the upstream roughness elements for large  $p/k$ . One interpretation is that the decreasing normalized turbulence intensity at the log region is caused by the relaxation process when the flow travels a long distance after the upstream square bar.

The variations of  $C_f$  and  $\Delta U^+$  against the pitch ratio  $p/k$  are shown in Fig. 11. The reference results from DNS studies at low friction Reynolds number  $Re_\tau \approx 600$  [35,39] are compared with the present results with higher  $Re_\tau$ . The present data and the reference result show similar trends for  $C_f$  and  $\Delta U^+$ , where both parameters reach maximum values at  $p/k = 8$ . The value of  $C_f$  is lower than the DNS results, and  $\Delta U^+$  is higher than the DNS results for the entire range of  $p/k$ . Also, the variations of both parameters are relatively small for the regime of  $p/k = 4-16$  in comparison with the DNS results. Choi *et al.* [47] suggested the values of  $\Delta U^+$  and  $C_f$  decrease with increasing  $\delta_{99}/k$ . Here  $\delta_{99}/k$  spanned ranges 16–22 and 31–53 for the reference studies and the present results, respectively. Therefore, the fact that both parameters of  $C_f$  and  $\delta_{99}/k$  become less sensitive with the pitch ratio is attributed to the higher  $Re_\tau$  and  $\delta_{99}/k$ .

Figure 12 shows the velocity defect profile and the outer-scaled turbulence intensity for results in Table II. The top row [Figs. 12(a) and 12(b)] shows the smooth-wall case and the rough-wall cases with  $p/k = 2, 4$  and  $8$ , and the bottom row [Figs. 12(c) and 12(d)] shows the smooth-wall case and the rough-wall cases for  $p/k = 8-128$ . The velocity defect profiles in Figs. 12(a) and 12(c) show that all the rough-wall cases collapse well with the smooth-wall reference cases from  $y^*/\delta_{99} \approx 0.03$ .

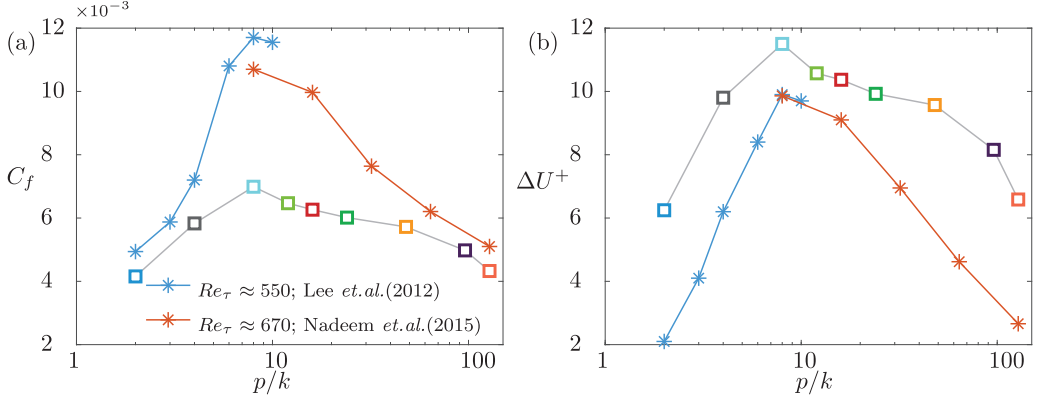


FIG. 11. Variations of  $C_f$  (a) and  $\Delta U^+$  (b) with different  $p/k$  for the present result (squares) and the DNS results (stars) of Lee *et al.* [39] and Nadeem *et al.* [35]. Symbols of the present results are defined as per Table II.

The collapse of the matching  $Re_\tau$  cases is similar to the cases in Sec. III, in which the matching pitch ratio cases also collapse well. Again, this collapse indicates that the assumption of the outer-layer similarity in the velocity defect law for other pitch ratio configurations is appropriate.

The situation is slightly different for the outer-scaled turbulence intensity shown in Figs. 12(b) and 12(d). All rough-wall data start to merge at  $y^*/\delta_{99} \approx 0.4$ , which is slightly farther than the farthest outer-layer peak of the case of  $p/k = 128$ . However, the difference at this location still spans the range  $\overline{u}^2/U_\tau^2 \leq 0.8$  ( $\leq 22\%$ ). The cases of  $p/k = 2, 4$  [Fig. 12(b)] and 48–128 [Fig. 12(d)] collapse well and show an excellent agreement at  $y^*/\delta_{99} \approx 0.4$ , with a small difference of  $\approx 6\%$ . For  $p/k = 8-24$  [Fig. 12(d)], the profiles show higher normalized turbulence intensity than the other pitch ratio configurations and the increase spans from 10% to 22%. The case of  $p/k = 12$  experiences the maximum increase of normalized turbulence intensity, which is two times larger than the uncertainty range caused by the  $U_\tau^2$  scaling. This outcome indicates that such higher normalized turbulence intensity is partially attributed to the roughness effects, not just resulting from the  $U_\tau^2$  scaling uncertainty. The cases of  $p/k = 8-24$  collapse with the other rough-wall results farther from the wall at  $y^*/\delta_{99} \approx 0.7$ , where the difference is reduced to  $\approx 10\%$ . Also, the normalized turbulence intensity increases with decreasing  $p/k$  from  $p/k = 24$  to 12 at  $y^*/\delta_{99} = 0.5$ , which supports the notion that such higher normalized turbulence intensity for  $p/k = 8-24$  is not just the result of  $U_\tau$  uncertainty, but is also associated with the roughness effects induced by pitch ratios. The DNS results of Lee *et al.* [39] and Nadeem *et al.* [35] also reported that the rough-wall cases of  $p/k = 8, 10$ , and 16 have higher normalized turbulence intensity compared to the other rough walls with  $p/k < 8$  and  $p/k > 16$ , where the increases reach  $\overline{u}^2/U_\tau^2 \approx 0.2$  at  $y^*/\delta_{99} \approx 0.5$ .

The rough walls with  $p/k = 2, 4$ , and 48–128 are considered as the d-type roughness with dense pitch ratios of  $p/k \leq 4$  [28] and sparsely rough walls with  $p/k \geq 32$  [35], respectively. Lee *et al.* [39] and Macdonald *et al.* [31] have suggested that the flows over d-type roughness show a similarity to the smooth-wall TBL, which is also reported for the sparsely rough walls by Nadeem *et al.* [35]. For the present results, the rough-wall cases of  $p/k = 2, 4$  and 48–128 show better agreement from  $y^*/\delta_{99} = 0.4$  in Figs. 12(b) and 12(d), respectively, compared with the interval range of  $p/k = 8-24$ . Although this observation is affected by the  $U_\tau$  uncertainty, it is believed that the pitch ratios around  $p/k = 12$  have stronger roughness effects than the d-type and sparsely rough walls in the outer layer. In Table II, the analysis of  $\delta_{99}/k$  and  $\delta_{99}/K_s$  shows that the rough-wall cases of  $p/k \leq 4$  and  $p/k \geq 48$  show more pronounced similarity in the outer layer, correlating with higher values of  $\delta_{99}/K_s$  rather than the typical ratio of  $\delta_{99}/k$ . This result suggests that for 2D roughness TBLs, the  $K_s$  appears to be a more appropriate length scale to examine the outer-layer

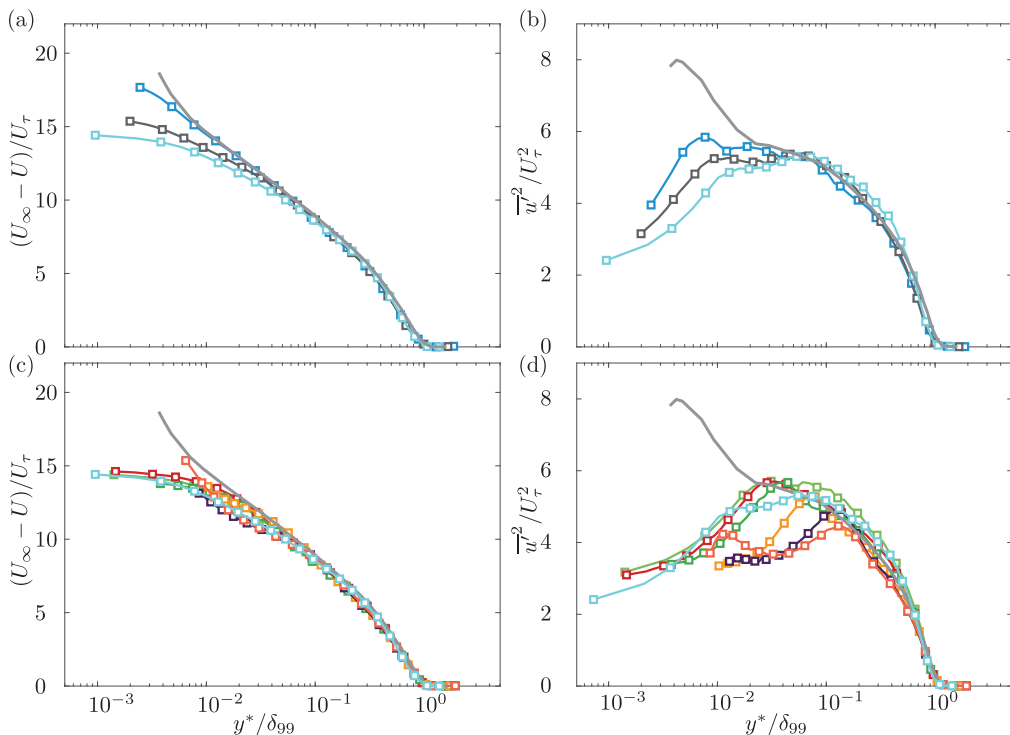


FIG. 12. Comparison of the 2D roughness with  $p/k = 2$  to 128 at  $\text{Re}_\tau \approx 3500$  (refer color codes to Table II) and the smooth-wall TBL from Örlü *et al.* [90],  $\text{Re}_\tau = 3500$  (gray solid line). Mean velocity defect for  $p/k \leq 8$  (a); outer-scaled turbulence intensity profile for  $p/k \leq 8$  (b); mean velocity defect for  $p/k \geq 8$  (c); outer-scaled turbulence intensity profile for  $p/k \geq 8$  (d).

similarity. The ratio is suggested to be  $\delta_{99}/K_s > 18$  to provide support for the outer-layer similarity hypothesis.

Compared with the outer-scaled normalized turbulence intensity distributions from DNS studies for two ranges of  $p/k = 2\text{--}10$  [39] and  $8\text{--}128$  [35], the present results in Figs. 12(b) and 12(d) show a clearer difference in the near-wall and outer-layer peaks due to the benefit of higher friction Reynolds number. Due to the larger scale separation between the inner and outer regions, there is a plateau consisting of the near-wall and outer-layer peaks for the rough-wall case of  $p/k = 8$ , instead of a single peak observed from DNS studies [35,39].

### B. Spectra analysis

Energy spectra maps for the matched Reynolds number rough-wall cases with  $p/k = 2\text{--}128$  are shown in Fig. 13. Note that for matching  $\text{Re}_\tau$  purpose, they are compared to the smooth-wall spectra map from the experimental study of Örlü *et al.* [90] at friction Reynolds number  $\text{Re}_\tau \approx 3500$ . The comparison is made by highlighting three energy spectra levels,  $k_x \Phi_{uu}^+ = 0.5, 0.8, 1.1$ , for the rough walls (white isolines) and the smooth wall (black broken isolines).

For  $p/k = 2$  in Fig. 13(a), the rough-wall spectra map has an inner peak at  $y^{*+} \approx 15$  and  $\lambda_x^+ = 1000$ , which indicates the turbulent structures are still dominated by the similar near-wall cycle of streaks and the quasistreamwise vortices as the smooth-wall TBL [81]. Compared with the black isolines, the high-energy area ( $k_x \Phi_{uu}^+ = 1.1$ ) for the rough wall at the near-wall region becomes smaller due to the reducing energy distribution of larger-scale structures ( $\lambda_x^+ \geq 1000$ ) caused by the roughness disturbance. In addition, the normalized energy starts to be transferred to the log region

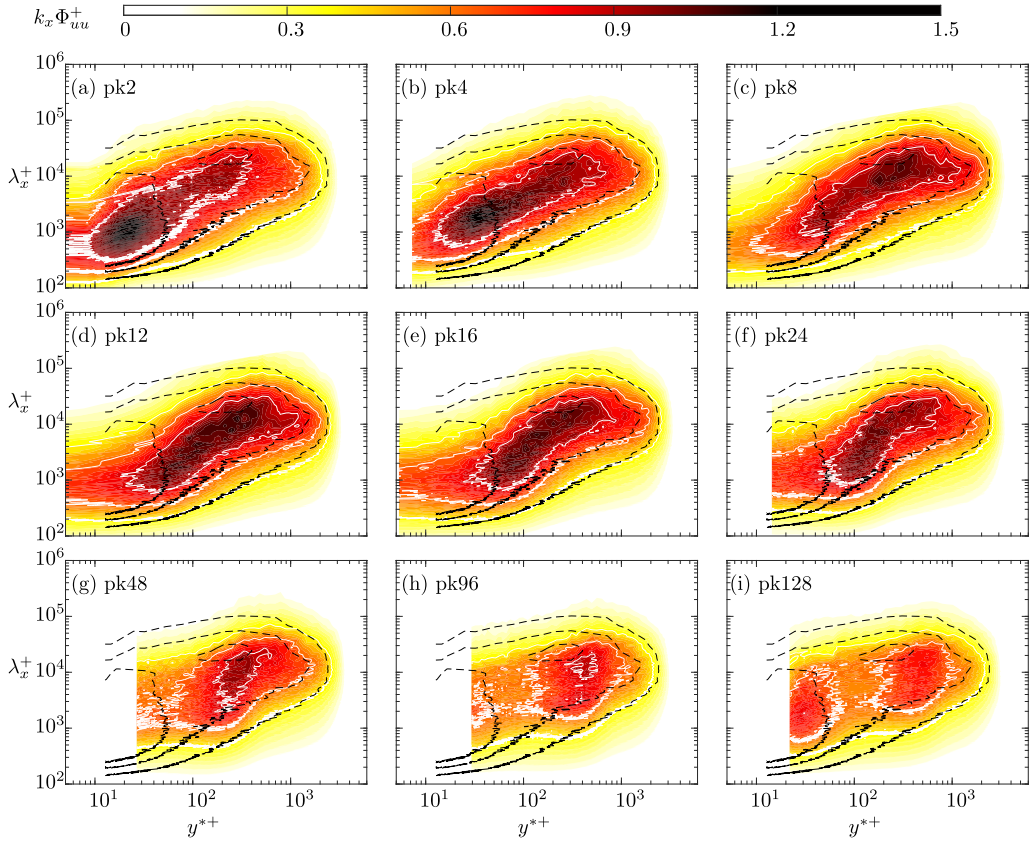


FIG. 13. Premultiplied spectra contour profiles for all 2D roughness result with  $p/k = 2-128$  for (a)–(i). The white and black isolines correspond to the rough- and smooth-wall cases with  $k_x \Phi_{uu}^+ = 0.5, 0.8, \text{ and } 1.1$ . The smooth-wall result are given by the experimental study of Örlü *et al.* [90] at similar friction Reynolds number  $Re_\tau \approx 3500$ .

where the high-energy area become larger. Comparing Figs. 13(a)–13(c) shows that the high-energy area ( $k_x \Phi_{uu}^+ = 1.1$ ) for the rough walls at the near-wall region shrinks and the inner-peak magnitude reduces with increasing  $p/k$ , which is consistent with the decreasing magnitude of the near-wall peaks in Fig. 10(b).

Figures 13(c)–13(f) show that the energy spectrum maps are similar for the rough-wall cases of  $p/k = 8-24$ , where the high-energy area stretches from the inner peak to the wake region. This observation is consistent with the normalized turbulence intensity profiles for  $p/k = 8-24$  in Fig. 12(d). In addition, comparing the active-energy areas ( $k_x \Phi_{uu}^+ = 0.8$ ) between the smooth and rough walls shows that the roughness effect extends to the wake region at  $y^{*+} \approx 2000$ , which is consistent with the deviation of turbulence intensities at the outer region  $y^*/\delta_{99} = 0.7$  for rough-wall cases  $p/k = 8$  to 24 in Fig. 12(d). This behavior suggests that for  $p/k = 8-24$  at this relatively high  $Re_\tau$ , more normalized energy is transferred up to the wake region and redistributed to all turbulent motions, compared with the DNS studies of Lee *et al.* [39] and Nadeem *et al.* [35]. A closer comparison shows the spectra map of  $p/k = 12$  has the largest high-energy area among the rough-wall cases  $p/k = 8$  to 24. A similar observation was made by Lee *et al.* [39], who reported that the streamwise velocity fluctuation is stronger for the 2D roughness case with  $p/k = 10$  than that of  $p/k = 8$  at  $Re_\tau \approx 600$ . It is well known that TBL flows over 2D roughness with  $p/k \geq 8$  can recover and approach reattachment to the bottom wall before it impinges on the following

elements, where the more organized flow near the bottom wall results in decreases of drag coefficient [34,38,39]. Here the more energetic near-wall motions for  $p/k = 12$  imply that more organized near-wall structures with the streamwise spacing of roughness elements larger than  $8k$  ( $k$  is the roughness height) can generate more normalized energy. However, when the streamwise spacing is more than  $16k$ , the near-wall structures contain less energy, which may result from the flow relaxation after traveling a distance longer than  $16k$ , as discussed in Sec. IV A.

In Figs. 13(g)–13(i), the white isolines show that the active-energy area starts shrinking for the rough-wall case of  $p/k \geq 48$  from the wall to the outer region. The outer peak decreases in magnitude with increasing  $p/k$ . The peak reduction is consistent with the normalized turbulence intensity development in Fig. 10(d). For the near-wall turbulent structures, the lower normalized energy appears for overall turbulent motions and becomes more severe with increasing  $p/k$  (up to  $p/k = 96$ ), which may be associated with the relaxation process. As expected, a pronounced inner peak emerges at  $y^{*+} \approx 40$  for  $p/k = 128$  because the near-wall structures that contain more normalized energy start redeveloping, similar to the smooth-wall TBL.

Compared with the smooth-wall isolines in Fig. 13, all rough-wall contours show that the largest-scale structures ( $\lambda_x^+ \geq 20,000$ ) have lower normalized energy from the wall to the log region  $y^{*+} \approx 400$ . This effect, caused by the roughness disturbance, monotonically weakens farther from the walls to the outer layer. The effect can even be seen in the rough-wall case of  $p/k = 128$ , which indicates the 2D roughness with a wide range of pitch ratios can reduce energy distribution of the largest-scale motions.

Figure 14 shows the energy spectra from Fig. 13 at two wall-normal locations of  $y^{*+} \approx 44$  and  $y^*/\delta_{99} \approx 0.06$ , corresponding to the near-wall and log regions. The plots are divided into two ranges of  $p/k$ , separated by  $p/k = 24$  because the spectra contours of  $p/k \leq 24$  are similar, where the left panel [Figs. 14(a) and 14(c)] shows the rough-wall cases with  $p/k = 2$ –24, while the right panel [Figs. 14(b) and 14(d)] shows the rest rough-wall cases of  $p/k = 48$ –128. In Fig. 14(a) the comparison between the smooth- and rough-wall cases shows the larger-scale structures with  $\lambda_x^+ \geq 6000$  encounter the reduction of the normalized energy. The collapse for rough-wall cases of  $p/k = 16$  and 24 indicates the roughness effect reaches a maximum with  $p/k = 16$ . As the energy modulation on the small-scale structures ( $\lambda_x^+ < 1000$ ) is similar and the hot-wire spatial resolution for these rough-wall cases varies slightly from  $l^+ = 24$  to 36, it is hard to determine the pitch ratio effect on the small-scale motions.

For larger pitch ratios  $p/k$ , Fig. 14(b) shows the turbulent structures with wavelengths  $\lambda_x^+ \leq 6000$  have significant normalized energy reduction when  $p/k$  increases from 24 to 48, but the larger-scale structures are slightly affected. Such lower normalized energy is related to the normalized turbulence intensity reduction in Fig. 12(d), which indicates that the relaxation process can reduce turbulence energy distribution on the turbulent motions with wavelengths  $\lambda_x^+ \leq 6000$ . In addition, the spectrum profile for  $p/k = 128$  is higher than that of  $p/k = 48$ –96, revealing that the re-emerging near-wall peak of the normalized turbulence intensity result is associated with the normalized energy growth on the overall turbulent motions. The peak close to  $\lambda_x^+ \approx 1500$  is due to forming of the near-wall cycle of streaks and quasistreamwise vortices near the bottom wall [63].

Figure 14(c) shows the rough walls of  $p/k = 2$ –24 have a similar energy modulation in the log region. Compared with the smooth-wall profile, the 2D roughness introduces more normalized energy to the turbulent structures at the wavelength range  $0.5 \leq \lambda_x/\delta_{99} \leq 6$  and reduces the normalized energy from the largest-scale structures ( $\lambda_x > 6\delta_{99}$ ). Again, the wavelengths of energy-growing turbulent structures indicate they are VLMS/superstructures [63,91]. Such energy modulation results in a similar normalized turbulence intensity at  $y^*/\delta_{99} = 0.06$  for  $p/k \leq 24$  in Figs. 12(b) and 12(d).

Figure 14(d) shows the largest-scale motions for the rough-wall cases of  $p/k \geq 24$  experience a similar normalized energy reduction compared with the smooth-wall result. In addition, the VLMSs ( $0.5 \leq \lambda_x/\delta_{99} \leq 6$ ) contain less energy with increasing  $p/k$  until  $p/k = 96$ , which indicates the energy stimulation to the VLMSs starts to weaken and the VLMSs are transitioning to that of the smooth-wall TBL from  $p/k = 24$  to 96. Such energy modulation implies the decrease of the

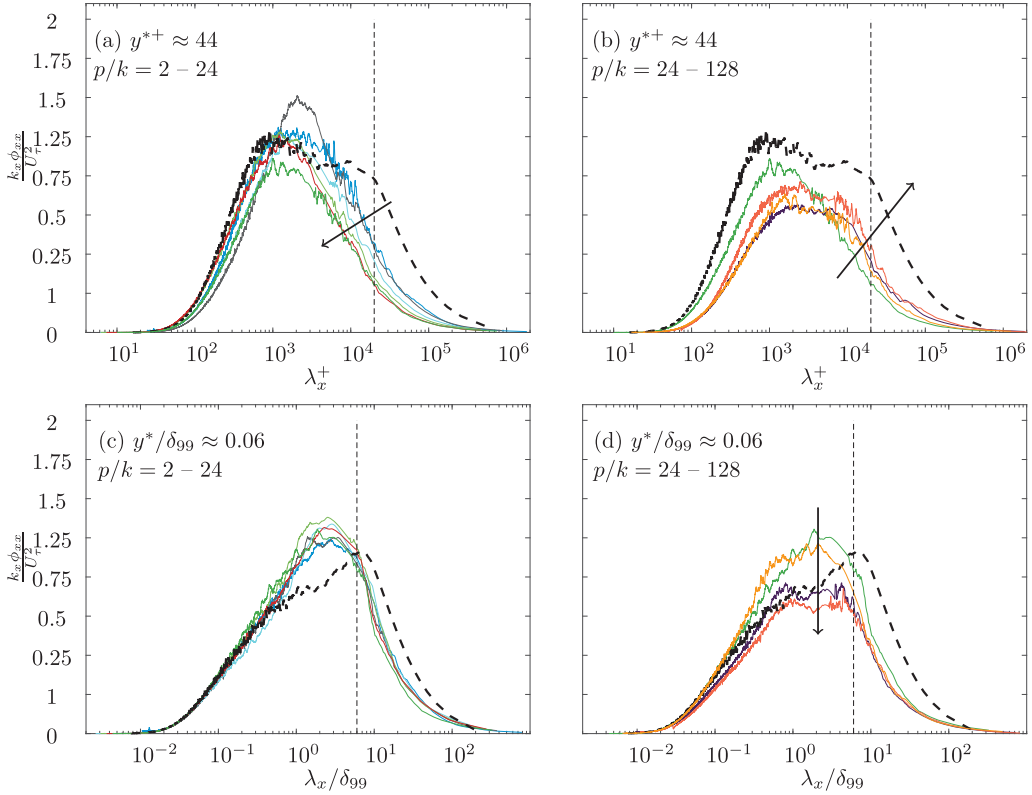


FIG. 14. Premultiplied spectra profiles in streamwise direction in variation of  $p/k$  for two wall-normal locations. The near-wall region at  $y^{*+} \approx 44$  for dense range of  $p/k = 2-24$  (a) and sparse range of  $p/k = 24-128$  (b); the log region at  $y^*/\delta_{99} \approx 0.06$  for the range of  $p/k = 2-24$  (c) and  $p/k = 24-128$  (d). Arrow indicates the increase of  $p/k$ . The vertical dash lines indicate the wavelength scales of  $\lambda_x^+ = 20\,000$  (a), (b) and  $\lambda_x/\delta_{99} = 6$  (c), (d). The smooth-wall result are black dash lines, referred to the same source as Fig. 13. The color code for all rough-wall cases are the same as per Table II without square markers.

normalized turbulence intensity for rough-wall cases of  $p/k \geq 24$  at  $y^*/\delta_{99} = 0.06$  [Fig. 12(d)] results from the normalized energy reduction on the VLMSs and largest-scale structures. Looking at all rough-wall spectra in the log region [Figs. 14(c) and 14(d)], the highly energetic VLMSs indicate 2D roughness with  $p/k = 2-48$  can cause VLMSs to become more energetic than for a smooth wall.

The normalized energy of the largest-scale motions ( $\lambda_x^+ > 20,000$  or  $\lambda_x/\delta_{99} > 6$ ) is indicated at the right side of the vertical dash lines in Fig. 14. Compared with the smooth-wall spectrum, analysis of the largest-scale motions at two wall-normal locations shows that the normalized energy for all rough-wall results is reduced throughout the log region and right down to the wall at  $y^{*+} \approx 44$ , which is also observed in the spectra contours for all rough-wall cases in Fig. 13. Similar observations were made in two previous roughness studies over a braille-type wall roughness [73] and sandpaper roughness [77]. The present results suggest that 2D square-bar roughness also modifies the largest-scale structures. In the near-wall region [Figs. 14(a) and 14(b)], the normalized energy of the largest-scale structures reduces with increasing pitch ratio from  $p/k = 2-12$  [black arrow in Fig. 14(a)] and increases with increasing pitch ratio from  $p/k = 24-128$  [black arrow in Fig. 14(b)]. For the log region [Figs. 14(c) and 14(d)], the normalized energy of the largest-scale structures is similar in magnitude for  $p/k \leq 24$  [Fig. 14(c)], but slightly decreases with increasing pitch ratio

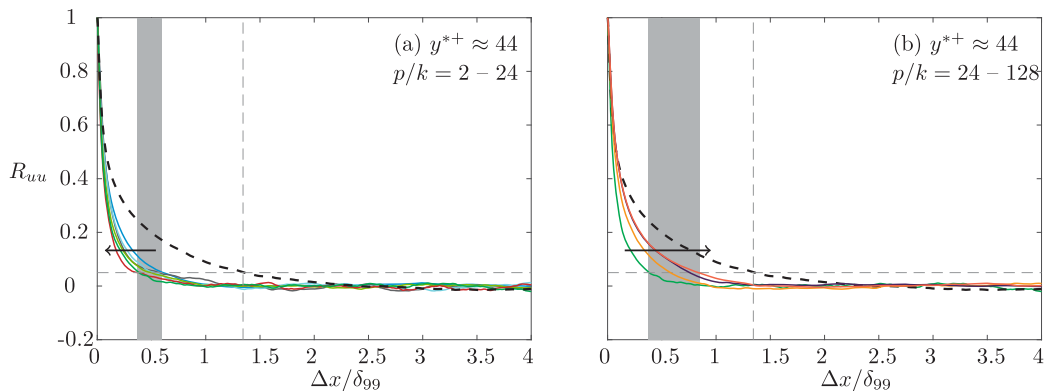


FIG. 15. Autocorrelations of the streamwise velocity fluctuation  $R_{uu}$  for the near-wall region at  $y^{*+} \approx 44$  for dense streamwise spacing range of  $p/k = 2-24$  (a) and sparse range of  $p/k = 24-128$  (b). The smooth-wall result are given by the experimental study of Örlü *et al.* [90], indicated by the black dash line. With the horizontal dash line at  $R_{uu} = 0.05$ , the average sizes of turbulent structures for the smooth-wall and various rough-wall cases are indicated by vertical dash lines and grey shaded bands, respectively. The black arrow indicates the increase of  $p/k$ . Color codes for rough-wall result are as per Table II.

for  $p/k \geq 48$  [Fig. 14(d)]. These observations suggest that the normalized energy reduction on the largest-scale structures by 2D roughness is associated with the pitch ratio in the near-wall region at the moderate Reynolds number  $Re_\tau = 3500$ . However, the pitch ratio influence becomes smaller farther away from the wall, at least to  $y^*/\delta_{99} \approx 0.06$ .

### C. Autocorrelation analysis

Figure 15 shows the autocorrelations of the streamwise velocity fluctuation  $R_{uu}(\Delta x, y_{\text{ref}})$  in two ranges of  $p/k = 2-24$  and  $p/k = 24-128$  in the near-wall region ( $y^+ \approx 44$ ). For both ranges, the rough-wall profiles are lower than that of the smooth wall, indicating 2D roughness shortens the average streamwise length of the near-wall structures over the range of pitch ratios  $p/k = 2-128$ . For the range  $p/k = 2-24$  [Fig. 15(a)], the black arrow indicates the increase of  $p/k$ , which shows the average length of turbulent structures reduces with increasing  $p/k$  and reaches a peak at  $p/k = 16$ . This outcome is the result of the energy distribution reduction of the large-scale structures ( $\lambda_x^+ \geq 6000$ ) as shown in Fig. 14(a). Contrasting behavior is observed for the range  $p/k = 24-128$  [Fig. 15(b)], where the black arrow indicates the average streamwise length of turbulent structures increases with increasing  $p/k$ . This outcome is associated with the reducing energy distribution on the small-scale structures for  $p/k = 24-48$  in Fig. 14(b).

Figure 16 shows autocorrelations at  $y^*/\delta_{99} = 0.06, 0.2$  for the log region and  $y^*/\delta_{99} = 0.5, 0.8$  for the wake region. All rough-wall results show a collapse with each other for four wall-normal positions. However, the scale reduction is severe for all rough-wall cases at  $y^*/\delta_{99} \approx 0.06$ , compared with that of the smooth wall. Towards higher wall-normal locations, the shaded band becomes smaller and closer to the vertical dashed line in Figs. 16(b)–16(d). This outcome indicates that in terms of the average length scale of the turbulent structures, all rough-wall cases show a good collapse with the smooth-wall result from the outer bound of the log region ( $y^*/\delta_{99} = 0.2$ ), and extending through the entire wake region. This observation implies that the scale of turbulent motions becomes independent of the pitch ratio  $p/k$  and provides support for the outer-layer similarity hypothesis on the average streamwise length of turbulent structures when  $y^*/\delta_{99} \geq 0.2$ .

Comparing the autocorrelation profiles from the near-wall region to the wake region in Figs. 15 and 16, the shaded bands show a trend that the average streamwise scale of turbulent structures increases from the wall up to the log region at  $y^*/\delta_{99} = 0.2$  with size  $\Delta x \approx 5\delta_{99}$  (twice the positively



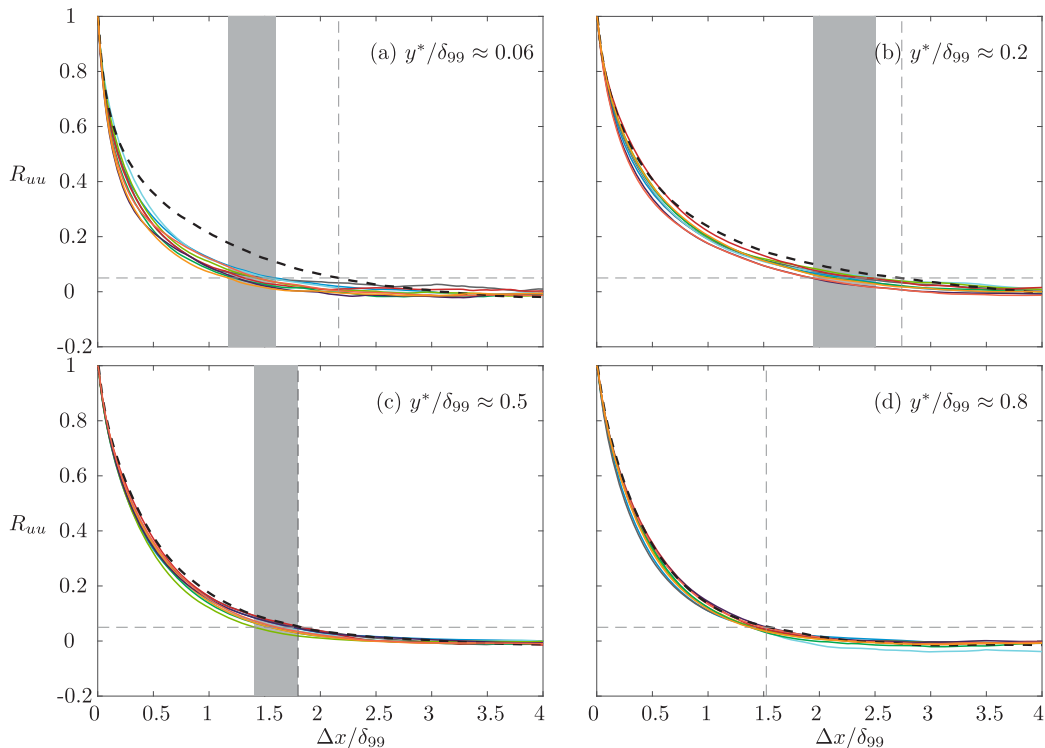


FIG. 16. Autocorrelation of the streamwise velocity fluctuation  $R_{uu}$  calculated at the outer coordinates,  $y^*/\delta_{99} = 0.06$ (a),  $y^*/\delta_{99} = 0.2$ (b),  $y^*/\delta_{99} = 0.5$ (c),  $y^*/\delta_{99} = 0.8$ (d). The smooth-wall result are given by the experimental study of Örlü *et al.* [90]. The black dash line is the smooth-wall result from literature [90]. Vertical dash lines and grey shaded bands indicate the average sizes of turbulent structures for the smooth- and rough-wall cases, respectively, as in Fig. 15. Color codes for rough-wall result are as per Table II.

correlated length). Farther from the log region, a shortening occurs and this scale approaches a constant in the wake region. This trend is consistent with the smooth-wall results of Hutchins and Marusic [63]. The streamwise length scale at zero crossing for the smooth- and rough-wall results ends at  $\Delta x = 3\delta_{99}$ , which is very close to the value of  $\approx 2.5\delta_{99}$  for the smooth-wall TBL reported by Hutchins and Marusic [63]. The matched streamwise length scale further supports the outer-layer similarity hypothesis on the streamwise length of turbulent structures.

## V. CONCLUSIONS

An experimental study was performed on 2D rough-wall TBLs, which consist of spanwise square bars, to investigate (1) Reynolds number effects for a pitch ratio defining classic k-type roughness ( $p/k = 8$ ) and (2) effects of the pitch ratio at a higher friction Reynolds number ( $Re_\tau \approx 3500$ ) than the existing (DNS) studies of Lee *et al.* [39] and Nadeem *et al.* [35].

The rough-wall results with  $p/k = 8$  and  $Re_\tau = 1840$ – $7500$  provided overall support for the outer-layer similarity hypothesis in forms of the normalized turbulence intensity, energy spectra and the autocorrelation, despite showing a slight discrepancy for the normalized turbulence intensity in the outer region between the smooth- and rough-wall data. It was interpreted that this deviation may be caused by the uncertainty of  $U_\tau$  scaling and the relatively low ratio of  $\delta_{99}/k \approx 50$ . As the friction Reynolds number increased, the drag coefficient was found to converge at  $C_f = 0.0068$ , when  $Re_\tau \geq 3900$  and  $\delta_{99}/k \geq 50$ . Further, the spectra contours suggested that more normalized

energy is transferred to the outer-region with increasing  $Re_\tau$ , but autocorrelation analysis showed that the streamwise scale of the turbulent structures is independent of friction Reynolds numbers from  $Re_\tau = 1840$ .

For the effect of the pitch ratio, both the drag coefficient and the roughness function were found to be greatest at  $p/k = 8$ . Compared with the DNS results at  $Re_\tau \approx 600$  with ratios  $\delta_{99}/k = 11$ – $26$  [35,39], the drag coefficient shows a weaker dependence on  $p/k$ , which was attributed to the higher friction Reynolds number  $Re_\tau \approx 3500$  and the higher range of ratio  $\delta_{99}/k = 31$ – $53$  for the present result. For the near-wall flow, the normalized turbulence intensity decreases with increasing  $p/k$  up to  $p/k = 96$  and has a near-wall peak at  $y^{*+} \approx 40$  when  $p/k = 128$ . The normalized turbulence intensity reduction for  $p/k = 2$  to  $24$  was mainly attributed to the roughness disturbance on the near-wall cycles and quasistreamwise vortices. A further intensity reduction for  $p/k = 24$  to  $48$  was interpreted to be related to the relaxation process. However, the influence of upstream roughness elements for the normalized turbulence intensity reduction remains unknown. In the outer region, the intensity profiles for rough walls with  $p/k = 8, 12, 16,$  and  $24$  were observed to be higher than the other rough-wall results. The maximum increase reaching two times larger than the uncertainty range of  $U_\tau$  scaling indicated that the pitch ratios around  $p/k = 12$  introduce stronger roughness effects to the normalized turbulence intensity in the outer layer.

The energy spectra contours and the autocorrelation profiles were used to analyze the effect of the pitch ratio on the turbulent structure in energy and streamwise length scale. An unexpected observation in the spectra contours showed that the reducing energy distribution of the largest-scale structures ( $\lambda_x^+ \geq 20\,000$ ) occurs from the log region and right down to the wall for all rough walls, even for the most sparsely rough wall ( $p/k = 128$ ). In addition, the autocorrelation results showed that the average streamwise scale of turbulent structures becomes independent of the pitch ratio above the log region.

In summary, 2D square-bar roughness experiments have been conducted with varying friction Reynolds numbers and pitch ratios. Data analysis revealed the drag behavior for the classic 2D roughness at a range of friction Reynolds numbers, and the pitch ratio effect to the 2D rough-wall TBL in terms of the mean statistics and the energy distribution. The more pronounced roughness effect for intermediate pitch ratios ( $p/k = 8$ – $24$ ) appeared to be associated with the turbulent structures in the wall-normal direction, such as the large-scale eruption events. This should motivate future work to collect data with vertical velocity components to give greater insights into the effects of the rough wall in this important regime.

## ACKNOWLEDGMENT

The authors wish to thank the Australian Research Council for financial support for this research.

## APPENDIX: THE FRICTION VELOCITY $U_\tau$ DETERMINATION TECHNIQUES

### 1. The composite profile method

The composite profile method, developed by Chauhan *et al.* [70], uses the composite function to fit with the measurement data for the turbulent boundary layer. The composite function comprising the Musker function  $U_{\text{inner}}^+$  [96] and the exponential function  $\mathcal{W}_{\text{exp}}$  [70], is given as

$$\frac{U}{U_\tau} = U_{\text{inner}}^+ + \frac{2\Pi}{\kappa} \mathcal{W}_{\text{exp}}\left(\frac{y}{\delta}\right), \quad 0 < y < \delta, \quad (\text{A1})$$

$$U_{\text{inner}}^+ = \frac{1}{\kappa} \ln\left(\frac{y^+ - a}{-a}\right) + \frac{R^2}{a(4\alpha - a)} \left\{ (4\alpha + a) \ln\left[ -\frac{a}{R} \frac{\sqrt{(y^+ - \alpha)^2 + \beta^2}}{y^+ - a} \right] \right. \\ \left. + \frac{\alpha}{\beta} (4\alpha + 5a) \left[ \arctan\left(\frac{y^+ - \alpha}{\beta}\right) + \arctan\left(\frac{\alpha}{\beta}\right) \right] \right\}, \quad (\text{A2})$$

where  $\alpha = (-1/\kappa - a)/2$ ,  $\beta = \sqrt{-2a\alpha + \alpha^2}$ ,  $R = \sqrt{\alpha^2 + \beta^2}$ ,  $a = -9.1867$  (for smooth wall), and

$$W_{\text{exp}} = \frac{1 - \exp\left[\frac{1}{4}(5a_2 + 6a_3 + 7a_4)\eta^4 + a_2\eta^5 + a_3\eta^6 + a_4\eta^7\right]}{1 - \exp[-(a_2 + 2a_3 + 3a_4)/4]} \left[1 - \frac{1}{2\Pi} \ln(\eta)\right], \quad (\text{A3})$$

where  $a_2 = 132.841$ ,  $a_3 = -166.2041$ ,  $a_4 = 71.9114$ , and  $\eta = y/\delta$ .  $\delta$  is the actual boundary layer boundary layer thickness as the point where the velocity profile reaches the free-stream velocity asymptotically. By fitting the measurement data from the wall to the free-stream flow, three parameters  $U_\tau$ ,  $\Pi$ , and  $\delta$  can be determined simultaneously.

## 2. The modified Clauser method

Perry and Li [97] derived the rough-wall boundary layer equation from the velocity defect profile as

$$\frac{U_\infty - U}{U_\tau} = -\frac{1}{\kappa} \ln\left(\frac{y - \epsilon}{\delta_{99}}\right) + \frac{2\Pi}{\kappa}. \quad (\text{A4})$$

By substituting  $\delta_{99} = (\kappa U_\infty \delta^*) / ((1 + \Pi)U_\tau)$  from [98] and rearranging, the rough-wall boundary layer equation is obtained as

$$\frac{U}{U_\infty} = 1 + \frac{1}{\kappa} \frac{U_\tau}{U_\infty} \ln\left(\frac{y - \epsilon}{\delta^*}\right) + \frac{1}{\kappa} \frac{U_\tau}{U_\infty} \ln\left(\frac{U_\tau}{U_\infty}\right) + \frac{1}{\kappa} \frac{U_\tau}{U_\infty} \ln\left(\frac{1 + \Pi}{\kappa}\right) - \frac{U_\tau}{U_\infty} \frac{2\Pi}{\kappa}, \quad (\text{A5})$$

where  $\kappa = 0.41$  and  $\Pi = 0.55$ , as suggested by 2D roughness DNS results [35,39]. Then the measurement data in the log-law region will be plotted in the form of  $U/U_\infty$  vs  $\ln(y^*/\delta^*)$  to fit with Eq. (A5). The friction velocity  $U_\tau$  and the offset of origin  $\epsilon$  are obtained.

- 
- [1] E. J. Richards, A review of aerodynamic cleanliness, *J. R. Aeronaut. Soc.* **54**, 137 (1950).
- [2] B. Nugroho, J. P. Monty, I. K. Utama, B. Ganapathisubramani, and N. Hutchins, Non-k-type behaviour of roughness when in-plane wavelength approaches the boundary layer thickness, *J. Fluid Mech.* **911**, A1 (2021).
- [3] I. K. Utama, B. Nugroho, M. Yusuf, F. A. Prasetyo, M. L. Hakim, I. K. Suastika, B. Ganapathisubramani, N. Hutchins, and J. P. Monty, The effect of cleaning and repainting on the ship drag penalty, *Biofouling* **37**, 372 (2021).
- [4] M. P. Schultz and G. W. Swain, The influence of biofilms on skin friction drag, *Biofouling* **15**, 129 (2000).
- [5] J. P. Monty, E. Dogan, R. Hanson, A. J. Scardino, B. Ganapathisubramani, and N. Hutchins, An assessment of the ship drag penalty arising from light calcareous tubeworm fouling, *Biofouling* **32**, 451 (2016).
- [6] T. Martin, M. Tsamados, D. Schroeder, and D. L. Feltham, The impact of variable sea ice roughness on changes in Arctic Ocean surface stress: A model study, *J. Geophys. Res. Oceans* **121**, 1931 (2016).
- [7] F. Hama, Boundary-layer characteristics for smooth and rough surfaces, *Trans. Soc. Nav. Archit. Mar. Eng.* **62**, 333 (1954).
- [8] D. Chung, N. Hutchins, M. P. Schultz, and K. A. Flack, Predicting the drag of rough surfaces, *Annu. Rev. Fluid Mech.* **53**, 439 (2021).
- [9] M. R. Raupach, R. A. Antonia, and S. Rajagopalan, Rough-wall turbulent boundary layers, *Appl. Mech. Rev.* **44**, 1 (1991).
- [10] J. Jiménez, Turbulent flows over rough walls, *Annu. Rev. Fluid Mech.* **36**, 173 (2004).
- [11] K. A. Flack and M. P. Schultz, Roughness effects on wall-bounded turbulent flows, *Phys. Fluids* **26**, 101305 (2014).
- [12] E. Napoli, V. Armenio, and M. De Marchis, The effect of the slope of irregularly distributed roughness elements on turbulent wall-bounded flows, *J. Fluid Mech.* **613**, 385 (2008).

- [13] R. J. Volino, M. P. Schultz, and K. A. Flack, Turbulence structure in a boundary layer with two-dimensional roughness, *J. Fluid Mech.* **635**, 75 (2009).
- [14] J. H. Lee, H. J. Sung, and P. Å. Krogstad, Direct numerical simulation of the turbulent boundary layer over a cube-roughened wall, *J. Fluid Mech.* **669**, 397 (2011).
- [15] L. Chan, M. Macdonald, D. Chung, N. Hutchins, and A. Ooi, A systematic investigation of roughness height and wavelength in turbulent pipe flow in the transitionally rough regime, *J. Fluid Mech.* **771**, 743 (2015).
- [16] T. O. Jelly and A. Busse, Reynolds number dependence of Reynolds and dispersive stresses in turbulent channel flow past irregular near-Gaussian roughness, *Int. J. Heat Fluid Flow* **80**, 108485 (2019).
- [17] J. Nikuradse, Laws of flow in rough pipes, Natl. Advis. Committee Aeronaut., Technical Memorandum 1292, November (NACA, Washington, DC, 1950).
- [18] K. Kevin, J. P. Monty, H. L. Bai, G. Pathikonda, B. Nugroho, J. M. Barros, K. T. Christensen, and N. Hutchins, Cross-stream stereoscopic particle image velocimetry of a modified turbulent boundary layer over directional surface pattern, *J. Fluid Mech.* **813**, 412 (2017).
- [19] P. Å. Krogstad and R. A. Antonia, Surface roughness effects in turbulent boundary layers, *Exp. Fluids* **27**, 450 (1999).
- [20] D. T. Squire, N. Hutchins, C. Morrill-Winter, M. P. Schultz, J. C. Klewicki, and I. Marusic, Applicability of Taylor's hypothesis in rough- and smooth-wall boundary layers, *J. Fluid Mech.* **812**, 398 (2017).
- [21] E. Hunke, W. Lipscomb, P. Jones, A. Turner, N. Jeffery, and S. Elliott, CICE, The Los Alamos Sea Ice Model (2017), <https://www.osti.gov/servlets/purl/1364126>.
- [22] M. Tsamados, D. L. Feltham, D. Schroeder, D. Flocco, S. L. Farrell, N. Kurtz, S. W. Laxon, and S. Bacon, Impact of variable atmospheric and oceanic form drag on simulations of Arctic sea ice, *J. Phys. Oceanogr.* **44**, 1329 (2014).
- [23] Y. Furuya, M. Miyata, and H. Fujita, Turbulent boundary layer and flow resistance on plates roughened by wires, *J. Fluids Eng. Trans. ASME* **98**, 635 (1976).
- [24] M. F. Tachie and K. K. Adane, PIV study of shallow open channel flow over d- and k-type transverse ribs, *J. Fluids Eng. Trans. ASME* **129**, 1058 (2007).
- [25] E. Sams, Experimental investigation of average heat transfer and friction coefficient for air flowing in circular tubes having square-thread-type roughness (National Advisory Committee for Aeronautics, 1952), Vol. RM E52D17.
- [26] A. E. Perry and P. N. Joubert, Rough-wall boundary layers in adverse pressure gradients, *J. Fluid Mech.* **17**, 193 (1963).
- [27] H. W. Townes and R. H. Sabersky, Experiments on the flow over a rough surface, *Int. J. Heat Mass Transf.* **9**, 729 (1966).
- [28] A. E. Perry, W. H. Schofield, and P. N. Joubert, Rough wall turbulent boundary layers, *J. Fluid Mech.* **37**, 383 (1969).
- [29] I. Tani, Turbulent boundary layer development over rough surfaces, in *Perspectives in Turbulence Studies*, edited by H. U. Meier and P. Bradshaw (Springer, Berlin, 1987), pp. 223–249.
- [30] S. Leonardi, P. Orlandi, and R. A. Antonia, Properties of d- and k-type roughness in a turbulent channel flow, *Phys. Fluids* **19**, 125101 (2007).
- [31] M. MacDonald, A. Ooi, R. García-Mayoral, N. Hutchins, and D. Chung, Direct numerical simulation of high aspect ratio spanwise-aligned bars, *J. Fluid Mech.* **843**, 126 (2018),.
- [32] L. Djenidi, R. Elavarasan, and R. A. Antonia, The turbulent boundary layer over transverse square cavities, *J. Fluid Mech.* **395**, 271 (1999).
- [33] S. Leonardi, P. Orlandi, L. Djenidi, and R. A. Antonia, Structure of turbulent channel flow with square bars on one wall, *Int. J. Heat Fluid Flow* **25**, 384 (2004).
- [34] S. H. Lee and H. J. Sung, Direct numerical simulation of the turbulent boundary layer over a rod-roughened wall, *J. Fluid Mech.* **584**, 125 (2007).
- [35] M. Nadeem, J. H. Lee, J. Lee, and H. J. Sung, Turbulent boundary layers over sparsely-spaced rod-roughened walls, *Int. J. Heat Fluid Flow* **56**, 16 (2015).
- [36] J. Cui, V. C. Patel, and C. L. Lin, Large-eddy simulation of turbulent flow in a channel with rib roughness, *Int. J. Heat Fluid Flow* **24**, 372 (2003).

- [37] S. E. Coleman, V. I. Nikora, S. r. McLean, and E. Schlicke, Spatial averaged turbulent flow over square ribs, *J. Eng. Mech.* **133**, 194 (2007).
- [38] S. Leonardi, P. Orlandi, R. J. Smalley, L. Djenidi, and R. A. Antonia, Direct numerical simulations of turbulent channel flow with transverse square bars on one wall, *J. Fluid Mech.* **491**, 229 (2003).
- [39] J. H. Lee, A. Seena, S. hyun Lee, and H. J. Sung, Turbulent boundary layers over rod- and cube-roughened walls, *J. Turbul.* **13**, N40 (2012).
- [40] A. A. Townsend, *The Structure of Turbulent Shear Flow*, 2nd ed. (Cambridge University Press, Cambridge, 1976), p. 429.
- [41] O. M. Bakken, P. Å. Krogstad, A. Ashrafian, and H. I. Andersson, Reynolds number effects in the outer layer of the turbulent flow in a channel with rough walls, *Phys. Fluids* **17**, 065101 (2005).
- [42] P. Å. Krogstad, H. I. Andersson, O. M. Bakken, and A. Ashrafian, An experimental and numerical study of channel flow with rough walls, *J. Fluid Mech.* **530**, 327 (2005).
- [43] A. Ashrafian, H. I. Andersson, and M. Manhart, DNS of turbulent flow in a rod-roughened channel, *Int. J. Heat Fluid Flow* **25**, 373 (2004).
- [44] A. Ashrafian and H. I. Andersson, Roughness effects in turbulent channel flow, *Prog. Comput. Fluid Dyn.* **6**, 1 (2006).
- [45] R. J. Volino, M. P. Schultz, and K. A. Flack, Turbulence structure in boundary layers over periodic two- and three-dimensional roughness, *J. Fluid Mech.* **676**, 172 (2011).
- [46] V. Efros and P. Å. Krogstad, Development of a turbulent boundary layer after a step from smooth to rough surface, *Exp. Fluids* **51**, 1563 (2011).
- [47] Y. K. Choi, H. G. Hwang, Y. M. Lee, and J. H. Lee, Effects of the roughness height in turbulent boundary layers over rod- and cuboid-roughened walls, *Int. J. Heat Fluid Flow* **85**, 108644 (2020).
- [48] L. Djenidi, R. A. Antonia, M. Amielh, and F. Anselmet, A turbulent boundary layer over a two-dimensional rough wall, *Exp. Fluids* **44**, 37 (2007).
- [49] S. K. Robinson, Coherent motions in the turbulent boundary layer, *Annu. Rev. Fluid Mech.* **23**, 601 (1991).
- [50] R. J. Adrian, Particle-imaging techniques for experimental fluid mechanics, *Annu. Rev. Fluid Mech.* **23**, 261 (1991).
- [51] R. J. Adrian, Hairpin vortex organization in wall turbulence, *Phys. Fluids* **19**, 041301 (2007).
- [52] A. J. Smits, B. J. McKeon, and I. Marusic, High-Reynolds number wall turbulence, *Annu. Rev. Fluid Mech.* **43**, 353 (2011).
- [53] J. Jiménez, Cascades in wall-bounded turbulence, *Annu. Rev. Fluid Mech.* **44**, 27 (2012).
- [54] B. J. McKeon, High Reynolds number turbulent pipe flow, Ph.D. thesis, Princeton University, 2003.
- [55] I. Marusic and J. P. Monty, Attached eddy model of wall turbulence, *Annu. Rev. Fluid Mech.* **51**, 49 (2019).
- [56] R. J. Adrian and J. Westerweel, *Particle Image Velocimetry* (Cambridge University Press, Cambridge, 2011), p. 586.
- [57] S. M. Islam, K. Haga, M. Kaminaga, R. Hino, and M. Monde, Experimental analysis of turbulent flow structure in a fully developed rib-roughened rectangular channel with PIV, *Exp. Fluids* **33**, 296 (2002).
- [58] L. Wang, J. Hejcek, and B. Sunden, PIV measurement of separated flow in a square channel with streamwise periodic ribs on one wall, *J. Fluids Eng. Trans. ASME* **129**, 834 (2007).
- [59] D. Pokrajac, L. J. Campbell, V. Nikora, C. Manes, and I. McEwan, Quadrant analysis of persistent spatial velocity perturbations over square-bar roughness, *Exp. Fluids* **42**, 413 (2007).
- [60] S. H. Lee, J. H. Kim, and H. J. Sung, PIV measurements of turbulent boundary layer over a rod-roughened wall, *Int. J. Heat Fluid Flow* **29**, 1679 (2008).
- [61] J. H. Lee, H. J. Sung, S. H. Lee, and K. Kim, Structures of the turbulent boundary layer over a rod-roughened wall, *Int. J. Heat Fluid Flow* **30**, 1087 (2009).
- [62] K. C. Kim and R. J. Adrian, Very large-scale motion in the outer layer, *Phys. Fluids* **11**, 417 (1999).
- [63] N. Hutchins and I. Marusic, Evidence of very long meandering features in the logarithmic region of turbulent boundary layers, *J. Fluid Mech.* **579**, 1 (2007).
- [64] A. E. Perry and M. S. Chong, On the mechanism of wall turbulence, *J. Fluid Mech.* **119**, 173 (1982).

- [65] P. M. Ligrani and P. Bradshaw, Subminiature hot-wire sensors: Development and use, *J. Phys. E: Sci. Instrum.* **20**, 323 (1987).
- [66] N. Hutchins, T. B. Nickels, I. Marusic, and M. S. Chong, Hot-wire spatial resolution issues in wall-bounded turbulence, *J. Fluid Mech.* **635**, 103 (2009).
- [67] R. J. Adrian, C. D. Meinhart, and C. D. Tomkins, Vortex organization in the outer region of the turbulent boundary layer, *J. Fluid Mech.* **422**, 1 (2000).
- [68] C. I. Chan, P. Schlatter, and R. C. Chin, Interscale transport mechanisms in turbulent boundary layers, *J. Fluid Mech.* **921**, A13 (2021).
- [69] C. C. Chin, N. Hutchins, A. S. Ooi, and I. Marusic, Use of direct numerical simulation (DNS) data to investigate spatial resolution issues in measurements of wall-bounded turbulence, *Meas. Sci. Technol.* **20**, 115401 (2009).
- [70] K. A. Chauhan, H. M. Nagib, and P. A. Monkewitz, On the composite logarithmic profile in zero pressure gradient turbulent boundary layers, AIAA 2007-532, *45th AIAA Aerospace Sciences Meeting and Exhibit* **9**, 6432 (2007).
- [71] F. H. Clauser, Turbulent boundary layers in adverse pressure gradients, *J. Aeronaut. Sci.* **21**, 91 (1954).
- [72] I. Marusic, J. P. Monty, M. Hultmark, and A. J. Smits, On the logarithmic region in wall turbulence, *J. Fluid Mech.* **716**, R3 (2013).
- [73] J. P. Monty, J. J. Allen, K. Lien, and M. S. Chong, Modification of the large-scale features of high Reynolds number wall turbulence by passive surface obtrusions, *Exp. Fluids* **51**, 1755 (2011).
- [74] K. A. Flack, M. P. Schultz, and J. S. Connelly, Examination of a critical roughness height for outer layer similarity, *Phys. Fluids* **19**, 095104 (2007).
- [75] M. P. Schultz and A. Myers, Comparison of three roughness function determination methods, *Exp. Fluids* **35**, 372 (2003).
- [76] J. M. Walker, The application of wall similarity techniques to determine wall shear velocity in smooth and rough wall turbulent boundary layers, *J. Fluids Eng.* **136**, 051204 (2014).
- [77] D. T. Squire, C. Morrill-Winter, N. Hutchins, M. P. Schultz, J. C. Klewicki, and I. Marusic, Comparison of turbulent boundary layers over smooth and rough surfaces up to high Reynolds numbers, *J. Fluid Mech.* **795**, 210 (2016).
- [78] R. J. Smalley, R. A. Antonia, and L. Djenidi, Self-preservation of rough-wall turbulent boundary layers, *Eur. J. Mech. B* **20**, 591 (2001).
- [79] S. Mochizuki, T. Kameda, and H. Osaka, Self-preservation of a turbulent boundary layer over d-type roughness, *J. Fluid Sci. Technol.* **1**, 24 (2006).
- [80] I. Marusic, K. A. Chauhan, V. Kulandaivelu, and N. Hutchins, Evolution of zero-pressure-gradient boundary layers from different tripping conditions, *J. Fluid Mech.* **783**, 379 (2015).
- [81] S. J. Kline, W. C. Reynolds, F. A. Schraub, and P. W. Runstadler, The structure of turbulent boundary layers, *J. Fluid Mech.* **30**, 741 (1967).
- [82] M. P. Schultz and K. A. Flack, The rough-wall turbulent boundary layer from the hydraulically smooth to the fully rough regime, *J. Fluid Mech.* **580**, 381 (2007).
- [83] L. Djenidi, K. M. Talluru, and R. A. Antonia, Can a turbulent boundary layer become independent of the Reynolds number?, *J. Fluid Mech.* **851**, 1 (2018).
- [84] I. Marusic, B. J. McKeon, P. A. Monkewitz, H. M. Nagib, A. J. Smits, and K. R. Sreenivasan, Wall-bounded turbulent flows at high Reynolds numbers: Recent advances and key issues, *Phys. Fluids* **22**, 065103 (2010).
- [85] K. A. Flack, M. P. Schultz, and J. M. Barros, Skin friction measurements of systematically-varied roughness: Probing the role of roughness amplitude and skewness, *Flow Turbul. Combust.* **104**, 317 (2020).
- [86] K. A. Flack, M. P. Schultz, J. M. Barros, and Y. C. Kim, Skin-friction behavior in the transitionally-rough regime, *Int. J. Heat Fluid Flow* **61**, 21 (2016).
- [87] G. I. Taylor, The spectrum of turbulence, *Proc. R. Soc. Lond. Ser. A* **164**, 476 (1938).
- [88] J. P. Monty, N. Hutchins, H. C. Ng, I. Marusic, and M. S. Chong, A comparison of turbulent pipe, channel and boundary layer flows, *J. Fluid Mech.* **632**, 431 (2009).

- [89] N. Hutchins and I. Marusic, Large-scale influences in near-wall turbulence, *Philos. Trans. R. Soc. A* **365**, 647 (2007).
- [90] R. Örlü, A. Segalini, J. Klewicki, and P. H. Alfredsson, High-order generalisation of the diagnostic scaling for turbulent boundary layers, *J. Turbul.* **17**, 664 (2016).
- [91] J. H. Lee and H. J. Sung, Very-large-scale motions in a turbulent boundary layer, *J. Fluid Mech.* **673**, 80 (2011).
- [92] N. Hutchins, W. T. Hambleton, and I. Marusic, Inclined cross-stream stereo particle image velocimetry measurements in turbulent boundary layers, *J. Fluid Mech.* **541**, 21 (2005).
- [93] I. P. Castro and E. Epik, Boundary layer development after a separated region, *J. Fluid Mech.* **374**, 91 (1998).
- [94] A. J. Smits, S. T. Young, and P. Bradshaw, The effect of short regions of high surface curvature on turbulent boundary layers, *J. Fluid Mech.* **94**, 209 (1979).
- [95] L. Ding and A. J. Smits, Relaxation of turbulent pipe flow downstream of a square bar roughness element, *J. Fluid Mech.* **922**, A34 (2021).
- [96] A. J. Musker, Explicit expression for the smooth wall velocity distribution in a turbulent boundary layer, *AIAA J.* **17**, 655 (1979).
- [97] A. E. Perry and J. D. Li, Experimental support for the attached-eddy hypothesis in zero-pressure-gradient turbulent boundary layers, *J. Fluid Mech.* **218**, 405 (1990).
- [98] D. Coles, The law of the wake in the turbulent boundary layer, *J. Fluid Mech.* **1**, 191 (1956).